Structure of β-crystallite assemblies formed by Alzheimer β-amyloid protein analogues: analysis by x-ray diffraction

Hideyo Inouye, Paul E. Fraser, and Daniel A. Kirschner
Neurology Research, Children's Hospital; and Department of Neurology, Harvard Medical School, Boston, Massachusetts 02115 USA

ABSTRACT To elucidate the relation between amyloid fibril formation in Alzheimer disease and the primary structure of the β/A4 protein, which is the major component of the amyloid, we have been investigating the ability of peptides sharing sequences with β/A4 to form fibrils in vitro. In previous studies we focused on the macroscopic morphology of the assemblies formed by synthetic peptides corresponding in sequence to different regions of this protein. In the present study we analyze the x-ray diffraction patterns obtained from these assemblies.

All specimens showed wide angle reflections that could be indexed by an orthogonal lattice of β-crystallites having unit cell dimensions $a \approx 9.4$ Å, $b \approx 7$ Å, and $c \approx 10$ Å, where *a* refers to hydrogen bonding direction, *b* to polypeptide chain direction, and *c* to intersheet direction. Given the amino acid sequence of β/A4 as NH_2-DAEFRHDSGYEVHHQKLVFFAEDVGSNKGAIIGLMVGGVVIAT-COOH, we found that, based on their orientation and assembly, the analogues could be classified into three groups: Group A, residues 19-28, 13-28, 12-28, 11-28, 9-28, 1-28, 1-38, 1-40, 6-25, 11-25 and 34-42; Group B, residues 18-28, 17-28, and 15-28; and Group C, residues 22-35 and 26-33. For Groups A and C, the sharpest reflections were (h00), indicating that the assemblies were fibrillar, i.e., elongated in a single direction. Lateral alignment of the crystallites in Group A account for its cross-β pattern, in which the hydrogen bonding (H-bonding) direction is the fiber (rotation) axis. By comparison, the β-crystallites of Group C had no preferential orientation, thus giving circular scattering. For Group B, the sharpest reflections were (h0l) on the meridian, indicating that the assemblies were plate-like, i.e., extended in two directions. A series of equatorial Bragg reflections having a 40 Å period indicated regular stacking of the plates, and the rotation axis was normal to the surface of the plates.

Of the Group A peptides, the analogues 11-28 and 6-25 showed intensity maxima on the equator as well as on higher layer lines, indicating that the β-crystallites are highly ordered relative to one another in the axial, H-bonding direction. This sampling of the layer lines by a larger period (60 Å) suggests that the β-crystallites are arrayed either in cylindrical or small restricted crystalline lattices. Consistent with its electron microscopic images, we modeled the structure as a tube with five or six β-crystallites constituting the wall and with the individual crystallite, which either rotates freely or is restricted, made of five or fewer β-pleated sheets. For the Group B peptides, the electron density projection along the *b*-axis was calculated from the observed intensities using phase combinations from β-keratin. Amino acid side-chain positions were apparent and, when refined as 4-Å-diameter spheres, led to a substantial decrease in the R-factors. For peptide 18-28 the electron density peaks, which are thought to correspond to side chains, were centered 3.3 Å from the peptide backbone, whereas for peptides 17-28 and 15-28, these peaks were centered 1 Å or more further from the backbone. Peaks having high electron density faced peaks having lower density, suggesting a favorable stereochemical arrangement of the residues. Thus, our analysis of the fiber x-ray patterns from β/A4 peptides shows the organization of the β-crystallites that form the wall of the amyloid fibrils as well as possible side-chain interactions.

INTRODUCTION

Electron microscopic and x-ray diffraction studies on synthetic polypeptide analogues of the β/A4 protein of Alzheimer disease (AD) have been carried out to elucidate the mechanism of amyloid fiber formation (Kirschner et al., 1987; Halverson et al., 1990; Fraser et al., 1991*a, b, c*). By studying fibrilogenesis of peptides corresponding to different regions of β/A4, one expects to understand the physical-chemical specificity of the amino acids and to clarify the minimum sequence necessary for fiber formation (also see Hilbich et al., 1991; Burdick et al., 1992). We previously showed (Kirschner et al., 1987) that the wide angle x-ray pattern of peptide 1-28 of β/A4 could be indexed by an orthogonal unit cell similar to that of β-keratin, except that the fiber axis was perpendicular to rather than parallel to the polypeptide chain direction, resulting in a cross-β rather than extended-β type diffraction pattern. The series of small-angle equatorial reflections were interpreted as arising from the interference between the β-crystallites constituting the walls of a slab-like or cylinder-like structure. Although these x-ray results were much more detailed than previous ones obtained from AD amyloid isolated from autopsy material (Kirschner et al., 1986), both the in vitro and purified material showed similar cross-β patterns. This suggested that the sequence 1-28 may be a major constituent of the tubular wall and prompted further studies on other peptide analogues of β/A4.

Since then, many additional analogues have been synthesized, and the x-ray diffraction data from their assemblies have been collected. Some of these assemblies are sufficiently well oriented to allow measurement of the intensity of their x-ray reflections for subsequent structural analysis. Although our previous reports focused largely on electron microscopic observation of macroscopic morphology, in the current study we describe our analysis of the x-ray patterns from the assemblies having

Address correspondence to Dr. Hideyo Inouye, Neurology Research, Enders 2, Children's Hospital, 300 Longwood Avenue, Boston, MA 02115.

Dr. Fraser's current address is Centre for Research in Neurodegenerative Diseases, Tanz Neuroscience Building, University of Toronto, Toronto Ontario M5S1A8, Canada.

0006-3495/93/02/502/18 $2.00

the highest degree of order—namely, the plate-like structures formed by certain of the shorter peptides and the fibrillar, amyloid-like structures formed by the intermediate length peptides. We analyzed the small-angle equatorial scattering to determine the sizes of the macromolecular aggregates and to model their organization based on the atomic coordinates of the β-sheet for β-keratin. For the plate-like assemblies, this modeling gives information about the side-chain interactions, whereas for the fibrillar structures, it indicates the organization of the β-crystallites in forming the tubular wall of the fibrils. Some of our results have been reported in abstract form (Inouye et al., 1991).

METHODS

Peptides and specimen preparation

The amino acid sequence of β/A4, numbered left to right from 1 to 43 is

NH_2-Asp-Ala-Glu-Phe-Arg-His-Asp-Ser-Gly-Tyr-Glu-Val-
1 2 3 4 5 6 7 8 9 10 11 12

His-His-Gln-Lys-Leu-Val-Phe-Phe-Ala-Glu-Asp-Val-
13 14 15 16 17 18 19 20 21 22 23 24

Gly-Ser-Asn-Lys-Gly-Ala-Ile-Ile-Gly-Leu-Met-Val-Gly-
25 26 27 28 29 30 31 32 33 34 35 36 37

Gly-Val-Val-Ile-Ala-Thr-COOH
38 39 40 41 42 43

The sources and sequence positions of the peptides were as follows: Peninsula Laboratories (Belmont, CA), 19-28, 17-28, 15-28, 13-28, 11-28, and 9-28; Star Biochemicals (Torrance, CA), 13-28 and 11-28; Dr. L. K. Duffy (University of Alaska, Fairbanks, AK), 18-28, 1-28, 1-38, 1-40, 6-25, and 22-35 (Kirschner et al., 1987; Fraser et al., 1991*a*, *b*); Dr. P. T. Lansbury (Massachusetts Institute of Technology, Cambridge, MA), 26-33 and 34-42 (Halverson et al., 1990); Dr. B. Frangione (New York University Medical Center, New York, NY), 17-28, 15-28, and 12-28; and the Biopolymers Laboratory, Harvard Medical School (Boston, MA), 11-25. Purity of the various peptides was determined by amino acid analysis and thin-layer chromatography. In the case of the Lansbury peptides, the purity was also verified by mass spectroscopy and proton nuclear magnetic resonance. As an additional purity check of the commercial peptides, we obtained proton nuclear magnetic resonance spectra (360 MHz) of them at the Francis Bitter Magnet Lab (Cambridge, MA). The spectra were consistent with the amino acid composition, and no extraneous or minor peaks were observed.

Lyophilized peptides were dissolved in glass-distilled water at 10 mg/ml and slowly dehydrated (at ambient humidity) in siliconized glass (or quartz) capillaries. The slight insolubility of peptides 17-28, 15-28 and 22-35 required 7–10% formic acid to produce clear solutions; dehydration of such solutions usually resulted in improved orientation of the final sample. Due to its high hydrophobicity, peptide 34-42 was dissolved in hexafluoroisopropanol and dried under a constant stream of hydrated nitrogen gas. In all cases, samples were dried in the presence of a 2-T, static magnetic field to induce orientation of the resulting assemblies. Further information about some of these assemblies, e.g., their morphology, tinctorial properties, solubility, and peptide conformation, has been published (Kirschner et al., 1987; Halverson et al., 1990; Fraser et al., 1991*a*, *b*, *c*).

X-ray diffraction

X-ray patterns were collected using nickel-filtered and double-mirror focused CuK_α radiation from a rotating anode x-ray generator (200 μm focal spot, model Elliott GX-20; GEC Avionics, Hertfordshire, England) operated at 35 kV and 35 mA. A helium tunnel was placed in the x-ray path to reduce air scatter. Patterns were recorded on flat direct-exposure x-ray film (Eastman Kodak Co., Rochester, NY) during exposure times of 1–3 d. The specimen-to-film distance ranged from 69 to 88 mm and was calibrated to ±0.05 mm using the known spacings of calcite and cholesterol. The Bragg spacings of reflections were measured either visually off the films using a 6× optical comparator or from digitized densitometer tracings.

The diffraction patterns were digitized using a photoscan (model P-1000; Optronics International, Chelmsford, MA) with either a 25-, 50-, or 100-μm raster. In most cases the intensities on the equator and meridian were circularly averaged within a defined angle. The direct beam dimensions were measured by linear scans along the meridian and equator. The background was defined by a polynomial curve before subtracting from the total intensity. Measurement of the integral widths for the observed peaks and for the incident beam was obtained by fitting the background corrected intensity profile to a Gaussian function. The actual fit to the observed peak was carried out by optimizing the input data (i.e., the peak height and half width) using a least-squares procedure.

The diffraction patterns from the various β/A4 analogues contained broad crystalline reflections as well as diffuse scatter (Fig. 1). To interpret these patterns, we developed procedures for analyzing fiber tilt, disorientation angles, disorder, and coherent size. Our detailed development of equations to accomplish this is included in the Appendix.

RESULTS AND INTERPRETATION

Description and classification of the x-ray diffraction patterns

The x-ray diffraction patterns that were analyzed in this article are shown in Fig. 1. The Bragg spacings, indexes of the reflections, and descriptions of the patterns from selected peptides (18-28, 17-28, and 11-28) are presented in Table 1. All diffraction patterns showed a strong wide angle reflection at 4.7 Å, which is characteristic of peptide chains in the β-conformation and corresponds to the distance between chains in the H-bonding direction. The meridional axis was defined to be in the direction of the 4.7-Å reflection and the equator perpendicular to it. All diffraction patterns showed a rotation axis either along the meridian or the equator, allowing the reflections on the rotation axis to be indexed one dimensionally and those on the other axis to be indexed two dimensionally. Based on their orientation and assembly, the analogues were classified into three groups. Group A consisted of the peptides that had the rotation axis parallel to the H-bonding direction: 19-28, 13-28, 12-28, 11-28, 9-28, 1-28, 1-38, 1-40, 6-25, 11-25, and 34-42. Group B peptides had the rotation axis parallel to the polypeptide chain direction: 18-28, 17-28, and 15-28. Group C peptides showed no or little orientation of the assemblies: 22-35 and 26-33.

Initial molecular model considerations

For Groups A and C the major reflections at Bragg spacings < 10 Å were largely due to reflections indexed by an

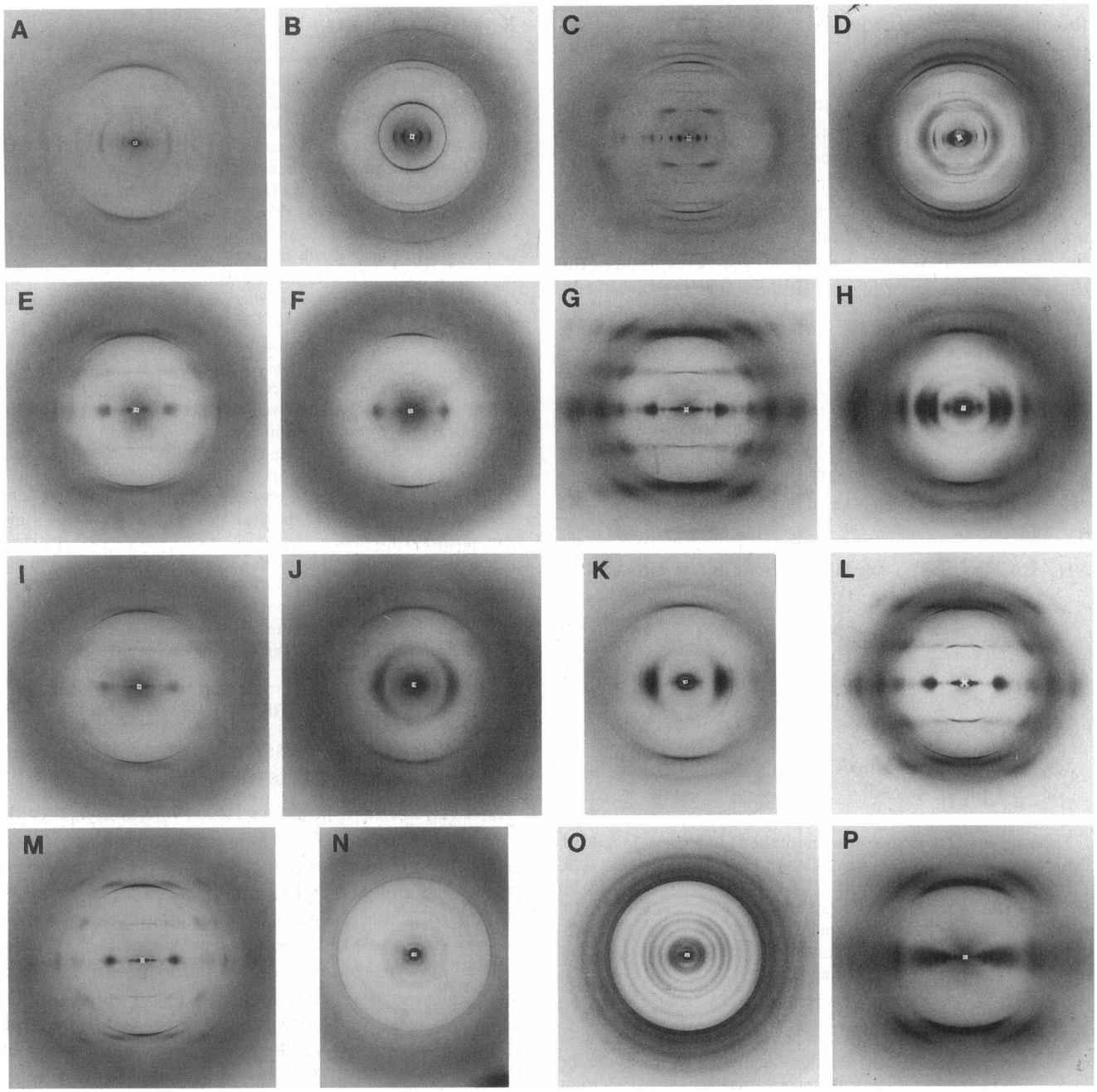

FIGURE 1 A gallery of representative x-ray diffraction patterns recorded from assemblies of synthetic peptide analogues of the Alzheimer β/A4 amyloid protein. (*A*) 19-28, Group A. This was the shortest peptide examined here that formed a cross-β fibril; however, such organized structures were formed only under very acid pH and did not show amyloid-like birefringence after staining with Congo red (Fraser et al., 1991*c*). Addition of one to four residues onto its amino-terminus resulted in a transition to ribbon-like structures (Fraser et al., 1991*c*). (*B*) 18-28, Group B; (*C*) 17-28, Group B; (*D*) 15-28, Group B; (*E*) 13-28, Group A; (*F*) 12-28, Group A; (*G*) 11-28, Group A. (*H*) 9-28, Group A. The three, small-angle peaks on the meridian were indexed by a 68.4-Å period. The wide-angle region was complex and showed many meridional reflections that could be indexed by a 47.4-Å period. (*I*) 1-28, Group A. The sample analyzed here gave very strong scattering near the origin, a broad, primary intensity maximum at 50.7 Å, and no multiple maxima in the 10-Å region. This differs somewhat from the one we had previously reported (Kirschner et al., 1987). In the latter one, the strong low-angle reflection was at 71 Å, and the intensity maximum at 10 Å was sampled by this large period. It appears that the β-crystallites in the current specimen do not form a regular cylindrical lattice (see detailed model calculation for 11-28 below) as the previous specimen did. Shrinkage or collapse of the cylindrical tube by dehydration could account for this difference. (*J*) 1-38, Group A; (*K*) 1-40, Group A; (*L*) 6-25, Group A; (*M*) 11-25, Group A; (*N*) 22-35, Group C. (*O*) 26-33, Group C. A monoclinic macrolattice was obtained assuming that the reflections with spacings larger than 5.9 Å are indexed as 0*kl*. (*P*) 34-42, Group A. Many wide-angle reflections on the equator are apparent. These are difficult to index for an orthogonal cell. A partially hydrated sample (not shown), however, showed a simpler pattern that contained broad intensity maxima centered at 22, 12, and 5 Å, the latter two of which correspond to (001) and (002) reflections. The orthogonal lattice constant for the β-crystallite was obtained assuming that $c \approx 10$ Å. Because the odd order layer lines are missing, the actual unit cell dimension along the *a*-axis may be 4.7 Å. Previously, the antiparallel conformation was proposed based on Fourier transform infrared spectroscopy (Halverson et al., 1990). These x-ray data, which suggest instead a parallel chain conformation, is consistent with the earlier observations that the inner strands of β-sheets are

orthogonal lattice having dimensions of $a \approx 9.4$ Å, $b \approx 7$ Å, and $c \approx 10$ Å, where a refers to H-bonding direction, b to polypeptide chain direction, and c to intersheet direction (Table 1). Visual estimate of the intensities roughly agrees with those calculated from the atomic coordinates of β-keratin (structure 2 in Fraser and MacRae, 1962) (also see Table 3 below), e.g., the very strong (001) and (200) reflections at ~10 and 4.7 Å, respectively, and the moderately strong (201) and (211) reflections at ~4.3 and ~3.6 Å, respectively (see Table 1 in Kirschner et al., 1987). For the analysis here, the wide-angle equatorial indexes for peptide 11-28 (Fig. 1 *G* and Table 1) will be presented below and compared with those based on the β-keratin model. A flow chart indicating the protocol of our analysis is presented as Fig. 2.

For Group B the meridional reflections were indexed two dimensionally by the unit cell $a \approx 9.4$ Å and $c \approx 10$–13 Å. Based on the atomic coordinates of β-keratin (see Table 3) the two-dimensional electron density projections were calculated (described below).

In this study we did not include the atomic coordinates for side chains except for the ones reported for β-keratin (α-carbon, β-carbon, carbon attached to oxygen, nitrogen, and oxygen); however, we did approximate side chains either as point atoms having N electrons or as spheres having radii r and average electron density ρ. The atomic scattering factor $f(R)$ in the former case is always N and in the latter case is given by $f(R) = 2\rho[\sin(ar)/a^2 - r \cdot \cos(ar)/a]/R$, where R is the radial coordinate in spherical coordinates and $a = 2\pi R$. The radii were assumed to be 2 Å, which is the averaged radius for different side chains of amino acids according to data compiled by Zimmerman et al. (1968).

Coherent domain size

Assuming that the observed intensity maxima and the incident x-ray beam are Gaussian, then the observed peak profile is a convolution of the incident beam, the coherent length, and the lattice disorder. The integral width of the observed reflection (δ_{obs}) is related to the integral widths of the direct beam b, coherent length Nd, and standard deviation of the second kind of lattice disorder δ (Inouye et al., 1989),

$$\delta_{obs}^2 = b^2 + (l/Nd)^2 + [d^{-1} \cdot \pi^2 \cdot h^2 \cdot (\delta/d)^2]^2,$$

where N is the number of lattice points, h is an index, and d is the one-dimensional period. Measurements of the integral width of the direct beam and the observed reflections give the lower limit of Nd value according to this equation when δ is assumed to be zero.

For Group A and C peptides the (h00) reflections were sharper than the (0kl) reflections, whereas for Group B the (h0l) reflections were the sharpest. The average ratios of coherent lengths in the H-bonding and intersheet directions were as follows: Group A, 8.7; Group B, 1.0; and Group C, 2.5 (Table 2). This indicates that scattering objects in Group A and C are elongated in the H-bonding direction, whereas in Group B they are plate-like, i.e., elongated in the H-bonding and intersheet directions. The cross-β fiber patterns from Group A peptides are, therefore, due to lateral alignment of the β-crystallites, whereas the circular scattering from Group C peptides arises from the lack of preferential orientation of its constituent β-crystallites. The distinctive Bragg reflections on the equator in Group B peptides indicate that the plates are stacked regularly, and the absence of Bragg peaks other than on the meridian and equator suggests that there is substantial azimuthal disorientation of the plates.

Equatorial reflections of Group A and C peptides

Among Group A peptides, the analogues 19-28, 11-28, 6-25, and 34-42 (Fig. 1, *A, G, L,* and *P,* respectively) gave many equatorial reflections at both low and wide angles that were approximately sampled by a single one-dimensional lattice (see Table 1 for 11-28 and Fig. 3). In cylindrically averaged intensities such as these, a small restricted crystalline lattice (Burge, 1961; Vainshtein, 1966) or a discrete cylinder (Waser, 1955) can give apparent one-dimensional reflections. In such models, the intensity maxima arise from peak positions x_j of the J_0 Bessel function in the former or the positions x_h of J_0^2 in the latter. The x_j and x_h are approximately linear to the order of peak j or h and are given by $x_j = \pi(8j + 1)/4$ and $x_h = \pi(4h + 1)/4$. For a small restricted crystal lattice, $x_j = 2\pi \cdot a \cdot R_j$, where a is the distance between lattice points and R_j is the reciprocal coordinate of peak j. For the discrete cylinder, $x_h = 2\pi \cdot r \cdot R_h$, where r is the radius of the tube, or center of mass of the wall, and R_h is the reciprocal coordinate of the peak position of order h. In either case a plot of the reciprocal coordinates of the peaks (R_j or R_h) as a function of the order of reflection (j or h) gives a linear curve whose slope corresponds to the inverse of the distance between the lattice points or to the diameter of the tubular structure. We found, in fact, that the equatorial reflections for peptides 19-28, 11-28, 6-25, and 34-42 gave linear curves (Fig. 3). The inverse of the

hydrophobic and the high proportion of Val and Ile, in particular, are in parallel β-sheets in protein crystals (Chothia, 1984). The abundance of these hydrophobic residues in β-sheets comes from the stereochemical restriction of these residues in an α-helix. The global energy calculation confirms also the parallel β-sheet conformation (Chou et al., 1983). On the second layer line the 3.9-Å reflection, indexed as (210), is strong unlike other analogues. Spacings measured from *B, C,* and *G,* for which detailed analyses are presented in this paper, are summarized in Table 1. Spacings for the other x-ray patterns shown here are available on specific request.

TABLE 1 **Summary of Bragg spacings from selected β/A4 analogues**

18-28 Group B		17-28 Group B		11-28 Group A			
a 9.38		*a* 9.55		*a* 9.44		*a'* 9.44	
b —		*b* —		*b* 6.92		*b'* 59.99	
c 10.36		*c* 12.89		*c* 10.76		*c'* 70.02	
						α' 110.02°	
R 0.13%		*R* 0.47%		*R* 1.18%		*R'* 1.09%	
Å		Å		Å			
10.36 (vsM)	(001)	12.81 (mM)	(001)	56.26 (vsE)	1		
5.18 (wM)	(002)	9.51 (wM')	(100)	30.37 (sE)	2		
4.69 (sM)	(200)	7.62 (mM)	(101)	21.61 (wE)	3		
4.56 (vwM)	(102)	6.47 (wM)	(002)	16.57 (wE)	4		
4.44 (wM)*		5.36 (mM)	(102)	14.37 (wE)	5		
4.26 (vwM)	(201)	4.78 (sM)	(200)	10.76 (sE)	6	(001)	
3.47 (mM)	(003)	4.32 (mM)	(003)	9.61 (mE)	7		
		3.94 (wM)	(103)	7.40 (vwE)	9		
38.35 (vsE)	1	3.20 (mM)	(203)	6.35 (vwE)	10		
21.57 (mE)*				5.45 (wE)	11	(002)	
18.71 (sE)	2			5.18 (vwE)	12		
12.53 (wE)	3			4.25 (mE)	15	(012)	
9.47 (wE)	4	38.35 (vsE)	1	3.51 (wE)	18	(020)	
		19.65 (sE)	2	3.32 (vwE)	19	(021)	
		12.70 (mE)	3	2.86 (vwE)	22	(022)	
		9.43 (mE)	4	9.15 (m1L)		(100)	
		7.84 (vwE)	5	8.71 (w1L)			
		5.53 (wE)	7	7.07 (w1L)		(101)	
		4.85 (wE)	11	6.15 (w1L)			
				5.40 (w1L)		(110)	
				4.94 (m1L)		(111)	
				4.39 (w1L)			
				3.92 (w1L)		(112)	
				4.72 (vs2L)		(200)	
				4.49 (m2L)		(201)	
				4.17 (vw2L)			
				3.90 (w2L)		(210)	
				3.66 (m2L)		(211)	
				3.18 (vw2L)		(212)	
				2.77 (vw2L)		(220)	
				3.10 (vw3L)		(300)	

a, *b*, *c* are the β-crystallite unit dimensions, in Å, of the orthogonal lattice; *a'*, *b'*, *c'*, and *α'* are the lattice constants for the monoclinic macrolattice; *R* and *R'* are the relative goodness of fit, in %, between the observed and calculated spacings for reflections of the β-crystallite (indexes shown in parenthesis) and for all tabulated reflections of the macrolattice; E, equator; M, meridian; M', off meridian; 1L, 2L, 3L, first, second, and third layer lines; vw, w, m, s, vs indicate increasing intensity from very weak, weak, moderate, strong, and very strong.

* This reflection is unlikely to have come from the β-crystallite. Due to the cylindrical rotation, some observed reflections arise from multiple reciprocal points. Positive Miller indexes whose calculated spacings are the closest to the observed ones are indicated here. Integers indicate the apparent one-dimensional indexes of the macrolattice (see text). A complete Table summarizing the corresponding data for the other x-ray patterns analyzed in this article is available from the authors on specific request.

slopes, i.e., *a* or 2*r*, were 64, 63, 56, and 63 Å, respectively. The restricted lattice, which is characterized by short- range order and long-range disorder, is likely to be monoclinic, since all the observed reflections, including those at low and wide angles, could be indexed by a larger unit cell (see Table 1 for 11-28 analogue).

For the other analogues, such sampling by a larger period was not apparent; however, a few reflections in the low-angle region were often observed (see Table 1). The low-angle equatorial scattering, which corresponds to the lateral direction of fibers in Group A, may arise from the form factor and the interference between the laterally packed fibrils in the partially dried samples. In analyzing the low-angle scattering at spacings > 10 Å (where atomic details are ignored), the unit structure was assumed to be cylindrically symmetric, as indicated by electron microscopy. The equatorial intensity $I(R)$ is proportional to $|F(R)|^2 \cdot Z(R)$. For a solid cylinder $F(R) = r_0 \cdot J_1(2\pi r_0 R)/R$, and for a tubular cylinder $F(R) = J_0(2\pi r_0 R)$. $Z(R)$, the interference function after cylindrical averaging, is $\Sigma_j \Sigma_k J_0(2\pi r_{jk} R)$, where $r_{jk} = |\mathbf{r}_j - \mathbf{r}_k|$ in cylindrical coordinates (Oster and Riley, 1952; Worthington and Inouye, 1985). The interference term $Z(R)$ never becomes zero and gives only a few reflections for a disordered lattice. Approximate values of the interfibrillar distance *a* were obtained from the primary peak according to $2\pi aR = 7.037$, which corresponds to the first J_0 peak position. We assumed that a sharp primary peak without strong scatter near the origin arose from the first peak of the interference function, whereas a broad peak with strong scatter near the origin arose from the first maximum of the structure amplitude, i.e., $2\pi r_0 R = 5.152$ and 3.770 for a solid and tubular cylinder, respectively. Subsequent small-angle peaks were assumed to be intensity maxima of the structure factors.

Calculations based on the position of the major equatorial peak for Group A and C analogues indicated a

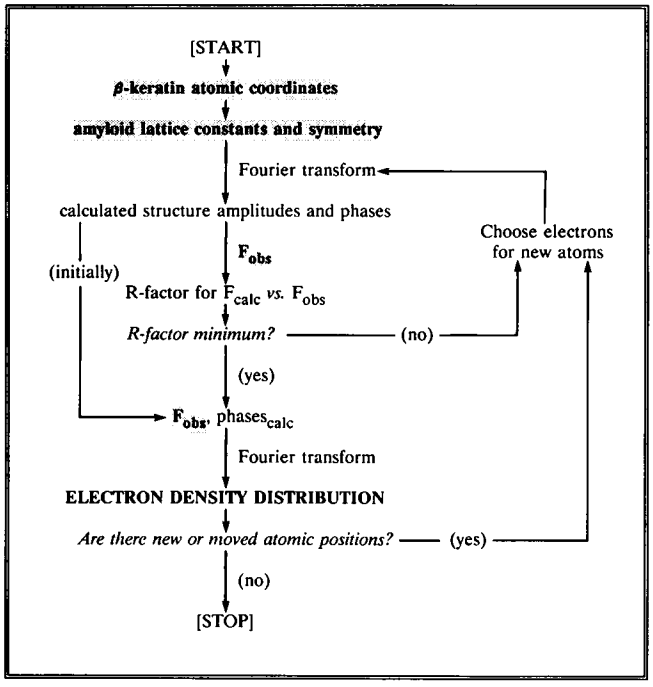

FIGURE 2 Flowchart indicating protocol for x-ray analysis of the wide-angle reflections from the β-amyloid analogues. The atomic coordinates from β-keratin was used with the lattice constants, and symmetry of the assemblies formed from the β-amyloid analogues and their observed structure amplitudes along either the meridian or the equator to calculate electron density projections. See text for details.

TABLE 2 **Measurement of coherent lengths and fibril widths**

Sample	d_{200}	d_{001}	$1/R_P$	Origin	Size
	Å	Å	Å		Å
19-28	150	73	50.5	Z	64
18-28	230	310			
17-28	440	410			
15-28	360	320			
13-28	440	32	46.7	Z	52
12-28	390	42	34.5	F	41 (57)
11-28	220	53	56.3	Z	63
9-28	170	68	43.4	Z	49
1-28	1,100	40	50.7	F	61 (84)
1-38	89	45	40.1	F	48 (66)
1-40	150	37	42.5	F	51 (69)
6-25	550	42	53.5	Z	56
22-35	210	56	33.4	F	40 (55)
26-33	170	61	54.1	Z	62
34-42	110	99	86.1	Z	63

The integral widths of the (200) and (001) reflections were measured to evaluate the coherent lengths in the H-bonding and intersheet directions, and the position of the primary low-angle reflection was used to estimate the widths of the fibrils (see Inouye et al., 1989, and text for details). The integral widths of the incident beam range from 0.0013 to 0.0033 $Å^{-1}$. The (200) Bragg spacings were in the range 4.67–4.82 Å, and (001) ranged from 9.84 to 13.81 Å. In most cases the integral widths of reflections related by symmetry were averaged. The error of the measured widths arising from the 50-μm raster size was 0.0005 $Å^{-1}$ for the specimen-to-film distance of 70 mm. R_P indicates the Bragg spacing for the primary low-angle peak, which originates either from interference (Z) or structure factor (F). Size denotes the estimated distance between fibrils (from Z) or estimated diameter of a tubular (or solid cylinder) (from F). For 19-28, 11-28, 6-25, and 34-42, the sizes were estimated from the linear regression curves (Fig. 3).

mean fibril width of 58 ± 11 Å (n = 17) (Table 2). This is within the range of widths observed by electron microscopy (Halverson et al., 1990; Fraser et al., 1991*a, b;* Burdick et al., 1992) but are about twofold larger than the 25–30-Å diameter of the subunits or subfibrils observed for assemblies of peptides 6-25, 1-28, 1-38, and 1-40.

Meridional reflections and axial twist in Group A assemblies

Although most of the peptides in Group A gave layer lines that indexed according to the unit dimension along the H-bonding direction (a = 9.4 Å), peptides 9-28 (Fig. 1 *H*) and 1-40 (Fig. 1 *K*) showed unique, low-angle reflections on the meridian. For 9-28, the first three meridional peaks were indexed by a 68.4-Å period. These reflections were elongated parallel to the equator, giving a diamond-shaped appearance. Such a shape, which is similar to that observed in DNA diffraction patterns (Marvin et al., 1961), may arise from helical twisting of the fiber. The wide-angle region in the x-ray pattern from 9–28 (Fig. 1 *H*) was complex and showed meridional reflections that could be indexed by a 47.4-Å period. Thus, the spacings at 9.47, 4.76, and 2.38 Å, which are indexed as 1st, 2nd, and 4th orders of a 9.47-Å period, also could be indexed as the 5th, 10th, and 20th orders of the 47.4-Å period.

In the 1-40 analogue (Fig. 1 *K*), a single, low-angle meridional reflection was detected at 53 Å and was observed to be elongated parallel to the equator. If the streak originates from a tubular or solid cylinder, then the radius is estimated to be 22 and 35 Å, respectively, values that are similar to those estimated from the low-angle, equatorial reflection (Table 2). The meridional reflection at 53 Å indicates a periodic structure along the H-bonding direction. Models that could account for the low-angle meridional reflections in peptides 9-28 and 1-40 are (*a*) a periodic arrangement of discrete objects along the fibril axis, (*b*) a staggered arrangement of subfibrils, and (*c*) twisting of the fibril. Axial arrangement of subunits with diameters of 25–30 Å, such as those that previously have been observed in thin sections of assemblies formed by the 13-28 analogue (Fraser et al., 1991*c*), could account for the meridional reflections.

The x-ray pattern from the 34-42 analogue (Fig. 1 *P*) showed both diffuse scattering and sharp reflections along the equator. The diffuse intensity, which modulated very smoothly, appeared to correspond to the Fourier transform that is sampled by the underlying sharp reflections. This suggests that the scattering unit is positioned on the lattice points and consists of several β-pleated sheets. The intensity showed pronounced fanning with a ~30° angle between the branches in the cross, indicating that the fibril may be twisted by 15° with respect to the meridional axis. Similar fanning of x-ray scattering has been reported for cellulose fibers (Heyn, 1948; Guinier and Fournet, 1955) and for collagen (Miller and Wray, 1971). When the fibril width is 63 Å (Table 2), its pitch would be 740 Å. Although the current x-ray camera setting did not resolve this reflec-

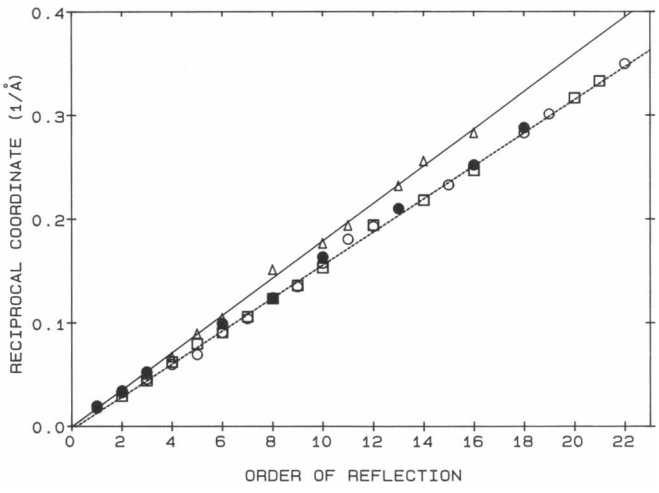

FIGURE 3 Plot of the reciprocal coordinates of the intensity maxima on the equator as a function of the order of reflection for 19-28 (●), 11-28 (○), 6-25 (△), and 34-42 (□) analogues. The linear regression curves (*solid,* peptide 6-25; *dashed,* 34-42) are shown.

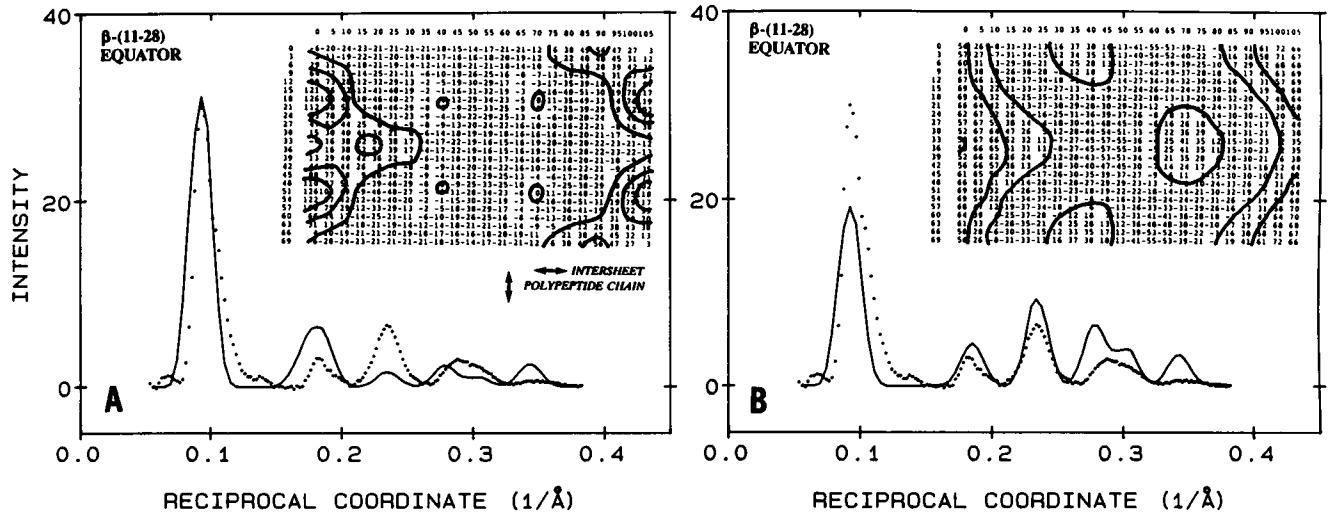

FIGURE 4 Wide-angle equatorial diffraction pattern from β/A4 analogue 11-28 (Fig. 1 *G*), and calculation of projected electron density in the plane of the intersheet and polypeptide chain directions. (*A* and *B*) Observed intensity (*dotted*) after background subtraction (where the intensity between the reflections was set to zero) and calculated intensity (*solid*) in the range of reciprocal coordinates ~0.053–0.38. The calculated intensity was obtained according to the procedure described in the Appendix. The intensity was initially calculated in the film space at intervals of 0.000466 $Å^{-1}$, assuming that there is no tilt and no disorientation of the fiber axis and that the disorder along the radial direction had an integral width 0.02 $Å^{-1}$. The curve was numerically averaged over a raster size of 500 μm and corrected using Lorentz and polarization factors (LP factors). Both curves were normalized so that the total area under the curve is one. In *A*, the calculated intensity was obtained from the atomic coordinates of β-keratin, and in *B*, it was from the refined model. Electron density distributions projected onto the *b*-*c* plane along the *a*-axis based on the original β-keratin model (*A inset*) and refined model (*B inset*) for 11-28 analogue. In *A inset*, the structure factors were calculated for $h = 0$ and $-3 \le k, l \le 3$. In *B inset*, the structure amplitudes used are from Table 4. The *b*-axis (0.3-Å step) is vertical, and the *c*-axis (0.5-Å step) is horizontal. The electron density is on a relative scale and calculated without F(000).

tion, electron microscopy on negatively stained fibrils does show a similar periodic deposition of stain (Halverson et al., 1990).

Electron density projection and β-crystallite organization of peptide 11-28

Among Group A peptides, analogue 11-28 gave well-oriented diffraction (Fig. 1 *G*). Sampling on the equator by a large period was apparent on the densitometer tracings. Using β-keratin as an initial model for defining phases, we analyzed the wide-angle equatorial scatter and derived an electron density projection onto the plane defined by the intersheet and chain directions (Fig. 4). The protocol for analyzing the wide-angle reflections is presented in Fig. 2. The low-angle equatorial intensity was used to analyze the organization of the β-crystallites in forming the macromolecular assembly (Fig. 5).

Wide-angle equatorial reflections

The strong reflections could be indexed two dimensionally, whereas the weak reflections appeared to arise from a long-range, macromolecular period of 63 Å (Table 2). The integral intensities for the peaks were measured after background subtraction. The structure amplitudes and phases were obtained by comparing the integral intensities and the structure factors calculated from the β-keratin model (Tables 3 and 4; Fig. 4 *A* and *inset*). The calculated intensity was assumed to be the sum of intensities of reflections whose spacings were within ±0.1 Å from the observed spacing. The Miller indexes used for the structure factor calculation were $h = 0$, $-3 \le k \le 3$, $-3 \le l \le 3$. The fiber tilt and disorientation were set to zero, since the observed equatorial intensity was averaged in the angular direction and the tilt angle was nearly zero. The Debye factor *B* was also set to zero.

The initial *R* factor between the observed and calculated intensities was $R_{\text{obs-amp}} = 42\%$ and $R_{\text{tot-amp}} = 71\%$. The two-dimensional, electron density projection revealed two peaks located at (*b*, *c*) coordinates (0, 3.6 Å) and (3.4 Å, 7.2 Å) (Fig. 4 *B, inset*). In a refined model, these new peaks were included and labeled as (*t*, *w*) (Table 3). Assuming these peaks to be point atoms, we optimized the number of electrons centered in the peak positions by searching in the range from 0 to 40 using increments of 10. The values giving the minimum *R* factor ($R_{\text{obs-amp}} = 35\%$) were 20 for both peaks (Fig. 4 *B, inset*). $R_{\text{tot-amp}}$ was 72%, and the total fit was not much improved. If the peaks were assumed to be spheres having radii of 2 Å, then the optimum values of their average electron densities were found to give the minimum $R_{\text{obs-amp}} = 35\%$ and $R_{\text{tot-amp}} = 69\%$. The electron density projection in either model revealed the same peak positions as determined from the point atom model. Although the chemical interpretation of the calculated electron density profiles is not yet established, qualitatively the new peak positions could correspond to large side chains, such as phenylalanine and histidine. Smaller

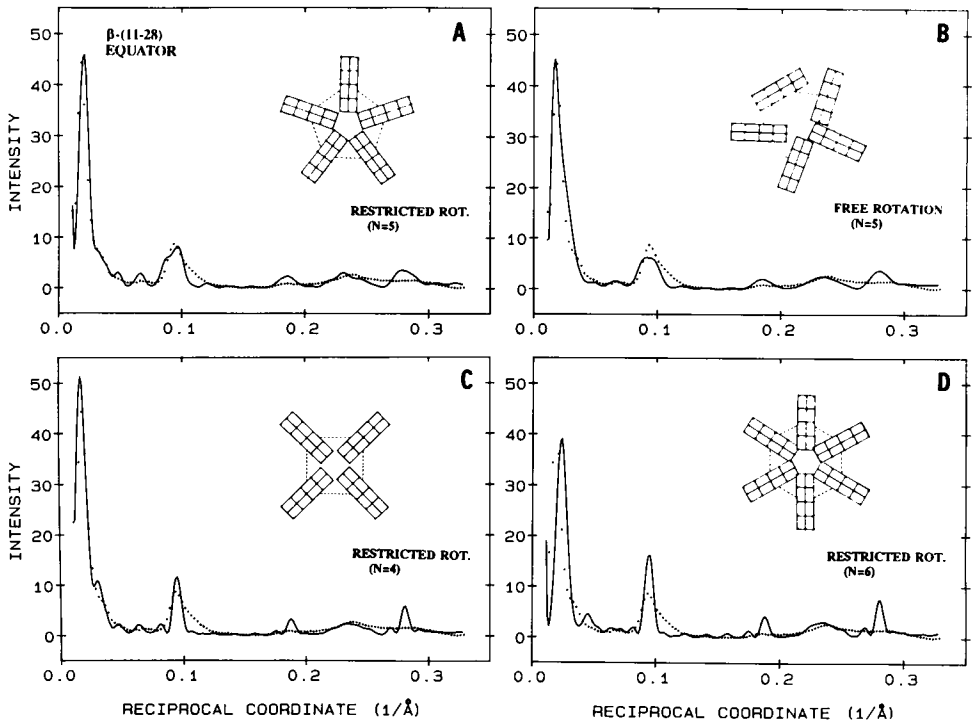

FIGURE 5 The observed (*dotted curve*) and calculated (*continuous curve*) low-angle, equatorial scatter from the assembly of peptide analogue 11-28. The calculated curves were based on the atomic coordinates as derived from the refined electron density profile (Fig. 4 *B, inset*) and the crystallite size positioned in cylindrical lattices having different numbers of lattice points, as depicted by the insets: (*A*) restricted rotation, $N = 5$; (*B*) free rotation, $N = 5$; (*C*) restricted rotation, $N = 4$; and (*D*) restricted rotation, $N = 6$. In all cases the radius of the cylindrical lattice was 32 Å. The total area of each intensity curve was normalized to unity. Since the calculated curve was obtained at every 0.00125 $Å^{-1}$, the observed curve was transformed to the same sampling, and the *R* factor was determined from the corresponding curves (see text for details).

residues would not account for the peak positions, which are located relatively far from the expected C_β position (Fig. 4 *B, inset*).

Macromolecular assembly of the β-crystallites

The equatorial intensity maxima including the low-angle scatter could be indexed by a one-dimensional lattice. How might β-crystallites, which have a limited size, be assembled into a cylindrical or a restricted crystalline lattice? In this section, we derive the equatorial intensity function by explicitly including refined atomic coordinates determined in the previous section. Electron microscopy (Fraser et al., 1991*a, c*) reveals that the fibril is a hollow tube having a diameter ranging from 50 to 100 Å and a circumference composed of five or six subunits. Therefore, in this text we chose a cylindrical lattice rather than a restricted crystalline lattice to account for the equatorial intensity. In the following the total intensity of atomic models in the cylindrical lattice was derived for two cases: when the rotation of the subfibril is free and when it is restricted (Fig. 5).

Free-rotation model of β-crystallites in cylindrical lattice. We assumed that the unit objects positioned on the planar lattice are random in angular distribution, whereas their centers remain exactly positioned at the lattice points. The intensity function in cylindrical coordinates after angular averaging in terms of the atomic coordinates is then

$$I(R, Z) = N\cdot(\langle F^2\rangle - \langle F\rangle^2) + \langle F\rangle^2\Sigma_j\Sigma_k J_0(2\pi r_{jk}R),$$
$$\langle F^2\rangle = \Sigma_m\Sigma_n f_m f_n J_0(2\pi r_{mn}R)\exp(i2\pi z_{mn}Z), \quad \text{and}$$
$$\langle F\rangle^2 = |\Sigma_m f_m J_0(2\pi r_m R)\exp(i2\pi z_m Z)|^2,$$

where N is the number of β-crystallites in the assembly, $\langle\ \rangle$ is the angular averaging operation, F is the Fourier transform of the β-crystallite, r_{jk} is the distance between the β-crystallites j and k in cylindrical coordinates, f is the atomic factor, and r_{nm} is the distance between atoms n and m of the crystallite measured in cylindrical coordinates (Vainshtein, 1966). These equations can be used for the intensity calculation from given atomic coordinates and unit cell dimensions. The Bessel function in the second term refers to the interference term after cylindrical averaging. On the equator, this function is written for a tubular hexagonal lattice made by six lattice points as $6 + 12\cdot J_0(2\pi aR) + 12\cdot J_0(2\pi\cdot 1.732\cdot aR) + 6\cdot J_0(4\pi aR)$. Similarly, for a tubular pentameric lattice with five lattice points, the function is $5 + 10\cdot J_0(2\pi aR) + 10\cdot J_0(2\pi\cdot 1.618\cdot aR)$. Regarding the tubular or hollow hexamer or pentamer as a discrete cylinder (Waser, 1955) allows the interference term to be written as $N^2\Sigma_n[J_{nN}(2\pi r_0 R)]^2$, for $-\infty \le n \le \infty$, where

TABLE 3 **Atomic coordinates of 11-28 analogue derived from equatorial scattering**

x	y	z	
0.041	0.007	−0.224	C_β
−0.008	0.000	−0.085	C_α
−0.059	0.322	0.019	C′
0.032	0.187	−0.019	N
−0.189	0.309	0.006	O
0.000	0.000	0.371	t
0.000	0.491	0.650	w

The equivalent asymmetric units were positioned at (x, y, z), ($-x$, $y + ½$, $-z$), ($-x + ½$, $-y$, z) and ($x + ½$, $-y + ½$, $-z$) as found for β-keratin (Fraser and MacRae, 1962). The electron density profiles were refined assuming that the t and w peaks are point atoms. The same t, w coordinates were also found when they were assumed to be spheres. The x-coordinates of t and w were set to zero since they are not determined from the equatorial scattering analysis. The atomic symbols C_β (β-carbon), C_α (α-carbon), C′ (carbon attached to oxygen), N (nitrogen), and O (oxygen) are indicated along the right. Note that these coordinates (given as fractions of the unit cell dimensions) were derived from the reported x, y, z coordinates in Å units of an orthogonal unit cell having a = 9.4 Å, b = 6.6 Å, and c = 10.5 Å (Fraser and MacRae, 1962).

N is the number of lattice points on the circle and r_0 is the radius of the circle. Selection of the maximum n (n_{max}) to limit the computation depends on the maximum R value (R_{max}) and the radius of cylinder (r_0). Because the first maximum of the $J_k(x)$ Bessel function is approximately at $x \approx k$, then $n_{max} = 2\pi r_0 R_{max}/N$. When $n < 0$, the Bessel term is obtained from $J_{-n}(x) = (-1)^n J_n(x)$. When n_{max} is correctly chosen, computation using the two different formulas for a cylindrical discrete lattice gave the same results.

Restricted-rotation model of β-crystallites in cylindrical lattice. When the β-crystallites form a macromolecular structure having N-fold rotation symmetry, the structure factors can be written in terms of atomic coordinates expressed in the cylindrical coordinate system. When the rotation of the β-crystallite is restricted and the crystallites are related to one another by rotational symmetry,

$$F(R, \Phi, Z) = N\Sigma_n\Sigma_j f_j J_n(2\pi r_j R) \times \exp\{i[n(\Phi - \phi_j + \pi/2) + 2\pi z_j Z]\},$$

where n = Nm, m is an integer, and j refers to atoms in the asymmetric unit. Because the macromolecules rotate, the observed intensity is the averaged FF^* in terms of angle Φ,

$$\langle I(R, \Phi, l/c)\rangle_\Phi = \Sigma_n(A_n^2 + B_n^2),$$

where

$$A_n = N\Sigma_j f_j J_n(2\pi r_j R)\cdot\cos\{n\cdot[\pi/2 - \phi_j] + 2\pi z_j Z\}, \text{ and}$$

$$B_n = N\Sigma_j f_j J_n(2\pi r_j R)\cdot\sin\{n\cdot[\pi/2 - \phi_j] + 2\pi z_j Z\}.$$

Numerical calculation from atomic models for equatorial scatter. In the models described above there are several unknowns, including whether the subfibril rotation is free or restricted and what values certain parameters have, such as size of the cylinder, number of subfibrils, numbers of β-pleated sheets, and number of residues along the β-strand. Because many of the parameters cannot be optimized easily by minimizing the difference between the observed and calculated intensities unless the input data are close to the correct values, we narrowed the possible ranges of the parameters by geometrical consideration.

First, from the integral width of the intersheet reflection at 10 Å spacing, a lower end of the coherent length along the intersheet direction, assuming zero lattice disorder, was estimated to be ~50 Å (Table 2). Thus, there must be about five lattice points along the c-direction. In the case of the free rotation model, the radius of the close-packed subfibril (r_s) was estimated to be 19 and 16 Å for N = 5 and N = 6, respectively, according to the equation $r_s = r_0 \sin(\pi/N)$, where r_0 is 32 Å (Table 2). These r_s values appear to be somewhat small given the ~50-Å coherent length of the β-crystallite in the c-direction, whereas the values are similar to the sizes of subfibrils estimated from electron micrographs. Sampling effects by a larger period were observed on higher layer lines, suggesting that the crystallites are likely correlated also in the H-bond direction. This indicates that the subfibrils may not rotate freely. In the restricted rotation model, the c-direction of β-crystallite was positioned to be radially oriented to account for the multiple intensity maxima or splitting at ~10-Å spacing. Assuming the five lattice points are along the c-direction, which corresponds to the length C of the rectangular lattice (see Fig. 5), the width B along the b-direction was estimated to be 17 and 14 Å for N = 5 and N = 6, respectively, according to $B = (2r_0 - C)\tan(\pi/N)$, where C is 40 Å and r_0 is 32 Å. These B values correspond to approximately three lattice points (i.e., a six residue repeat) along the b-direction. The β-crystallite size becomes ~20 Å along the b-axis and ~50 Å along the c-axis when atomic coordinates (defined in the unit cell) are placed on the lattice points.

We based the input atomic coordinates of the asymmetrical unit on the modified β-keratin (Table 3 and Fig. 4). We examined the equatorial intensities resulting from different numbers of lattice points (N = 4, 5, or 6) on the circumference with radius 32 Å. Total intensity curves were calculated with or without free rotation of the subunit crystallites, each having five lattice points along the c-axis and three lattice points along the b-axis (Fig. 5). All the calculated intensities with the restricted-rotation models closely fit the observed ones in overall shape and correctly reproduced the reflections indexed by an apparent one-dimensional lattice. Among them, the model with N = 5 gave the best fit (R = 32.9%) in comparison with the models of N = 4 (35.6%) and N = 6 (60.1%). The latter two models show a sharper intensity maximum at 10 Å, which arises from the exact direc-

tional alignment of the unit vectors of β-crystallite along the *c*-direction for opposed units. The free-rotation models of three different *N*s gave similar intensity curves, and the agreement between the observed and calculated intensities were 30.7, 32.2, and 31.5% for $N = 4$, 5, and 6, respectively. All models, however, smoothed out the intensity maxima and, therefore, did not reproduce the weak low-angle intensity maxima. We also calculated the equatorial intensity for the β-crystallites formed by five lattice points in the *b*-direction and three lattice points in the *c*-direction, which would be more consistent with the observed size of the subfibril by electron microscopy. For both free and restricted rotation crystallites with three different *N*s, the total intensity showed a much stronger 60 Å peak and intensity minimum at the position where the second reflection of 60 Å period was observed. All profiles, therefore, did not fit as well as those of the earlier models. The *R* factors for the restricted rotation models were 52.3, 45.7, and 61.6% and for the free-rotation models were 42.2, 41.7, and 47.5% for $N = 4$, 5, and 6, respectively.

Overall, according to the *R* factor, the intensity was best fit by the free-rotation model of β-crystallite having dimensions of ~20 Å along the *b*-axis and ~50 Å along the *c*-axis; however, this model failed to reproduce the weak, low-angle reflections. The restricted-rotation model having the above size of β-crystallite and $N = 5$ is a better model to explain the equatorial reflections. The calculated intensity maxima based on this model, however, were sharper than the observed maxima, suggesting that the angular rotation of β-crystallite is probably not completely restricted but partially disordered.

X-ray analysis of Group B (plate-like) assemblies

Sharp meridional reflections

The Group B peptides (18-28, 17-28, and 15-28) gave sharp meridional reflections (Figs. 1, *B–D* and Table 1). For analyzing these reflections, a similar protocol as for the wide-angle reflections of the 11-28 analogue was used (Fig. 2). Diffraction patterns from peptide 18-28 (Fig. 1 *B*) showed the (001) reflection as the strongest, similar to that calculated from β-keratin, whereas the patterns from the other two peptides showed (200) as the strongest reflection and (001) as much weaker (Fig. 6). As described in the Appendix, the structure amplitudes were obtained from the observed intensity proportionately divided by the calculated intensities having the same spacings as the observed reflection but having different indexes. Note that in our procedure the observed structure amplitude, therefore, depends on the structural model. The atomic coordinates of the model corresponded to the coordinates of β-keratin and, therefore, the fractional coordinates in the model were different from those of β-keratin because of slightly different cell dimensions. The phases as defined for the specific indexes were calculated from the model and assigned to the reflections having the same indexes. The *R* factors ($R_{\text{tot-amp}}$) were 28, 122, and 129%, respectively, for 18-28, 17-28, and 15-28 (see also Fig. 6). The corresponding $R_{\text{obs-amp}}$ were 28, 94, and 72%.

TABLE 4 Structure factors from equatorial pattern of Group A peptide 11-28

h	*k*	*l*	F_{obs}	F_{calc}	Phase	d_{obs}	d_{calc}
0	0	1	114.0	79.3	358.7	10.76	10.76
0	0	2	56.7	56.9	359.0	5.45	5.38
0	1	−2	78.5	67.2	84.5	4.25	4.25
0	1	2	79.1	67.8	273.7	4.25	4.25
0	0	3	58.1	89.0	4.7	3.51	3.59
0	2	0	19.2	29.4	355.7	3.51	3.46
0	2	−2	25.7	57.8	178.2	2.86	2.91
0	2	2	23.9	53.6	180.5	2.86	2.91

(*h*, *k*, *l*), Miller indexes; F_{obs}, observed structure amplitudes; F_{calc}, calculated amplitudes; phase, calculated phases in degrees; d_{obs}, observed spacings; and d_{calc}, calculated spacings. The $R_{\text{obs-amp}}$ is 35% and $R_{\text{obs-int}}$ is 60%. Note that reflections related by Friedel's law are not shown here. The relative error of the observed integral intensity is 4.8%, and arises from the deviation between the observed and calculated background intensity, approximated as polynomials.

For the peptides 17-28 and 15-28, it seemed at first that the *c*-axis corresponded to the chain direction because the 13-Å spacing was nearly twice the 7-Å chain repeat, and its intensity was much weaker than that of the first order intersheet reflection expected from the β-keratin model. The two-dimensional Patterson map (not shown), however, did not show the expected strong peaks at multiples of 3.3 Å along the *c*-axis. Therefore, we chose the *c*-axis to correspond to the intersheet direction. The electron density map was calculated from the phased structure factors without including the unobserved origin intensity. The projected electron density along the *b*-axis (Fig. 7) revealed four new peaks at positions other than those in the input atomic positions. The coordinates of the new peaks (denoted by *t*, *u*, *v*, and *w* in Table 5) were visually measured from the projected density. To refine the projection, we assumed that the peaks were either spheres (with a defined radius and average electron density) or point atoms (having all the electrons at the peak position). For the case of spheres, the radii were taken as 2 Å. The four parameters (t, u, v, and w) were varied independently in searching for a minimum *R* factor ($R_{\text{tot-amp}}$). During the refinement, the step size of the value assigned to the average electron density or to the number of electrons was gradually reduced, in parallel to the decrease in *R* factor. When $R_{\text{tot-amp}}$ did not change as a function of step size, new electron density profiles were calculated and new peak coordinates were chosen again. After the second or third iteration, $R_{\text{tot-amp}}$ reduced to 15, 28, and 40% in the former model (spheres) and to 17, 50, and 49% in the latter model (point atoms) for peptides 18-28, 17-28,

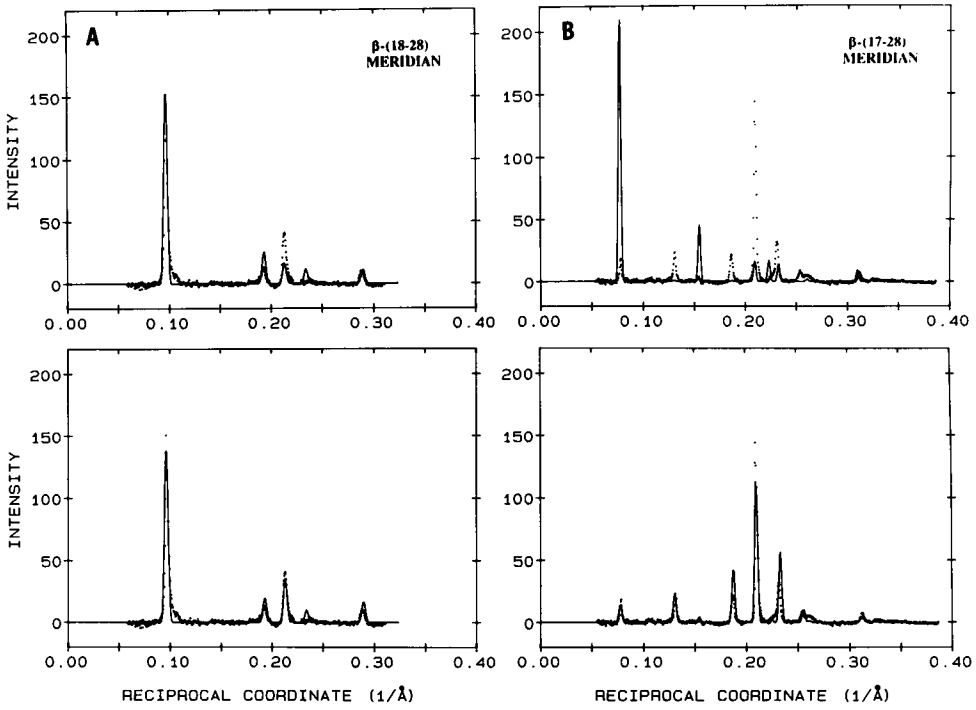

FIGURE 6 Observed (*dotted*) and calculated (*solid*) intensity on meridian for Group B homologues. (*A*) 18-28; (*B*) 17-28. The observed curves were after background subtraction. The LP factors were applied to the calculated curve rather than to the observed curve. Both observed and calculated curves were normalized so that the total area under each curve was unity. The calculated intensities, which are shown in the upper frames of *A* and *B*, were obtained from the atomic (fractional) coordinates of β-keratin. The refined calculated intensity curves are shown in the lower frames. The intensity was initially calculated in film space at intervals of 0.000466 $Å^{-1}$, assuming that the fibril axis is parallel to the *b*-axis and there is neither tilt nor disorientation of the fibrils. The input indexes were $-5 \leq h, l \leq 5$, and the *d*-spacings were larger than 3.0 Å. The reflection breadths for the calculated curves (ΔR) are 0.0043 $Å^{-1}$ for 18-28, 0.0028 $Å^{-1}$ for 17-28, and 0.0034 $Å^{-1}$ for 15-28. The curve was numerically averaged over a raster size of 100 μm.

and 15-28, respectively. The corresponding $R_{obs\text{-}amp}$ were 14, 16, and 28% for the former and 15, 29, and 29% for the latter models, respectively (Fig. 6, *A* and *B, lower,* and Tables 6 and 7). Thus, the sphere model gave smaller *R* factors, i.e., $R_{tot\text{-}amp}$, for all the indexable reflections.

The new peaks likely represent the positions of amino acid side chains (Fig. 7 and Table 5). The peak positions for 18-28 were much closer to the peptide backbone (3.3 Å) than those for 17-28 and 15-28 (4.2–4.8 Å), suggesting that smaller amino acid residues, probably Ala_{21}, Gly_{25}, and Ser_{26}, may largely constitute the β-crystallite in peptide 18-28. Support for this interpretation is provided by the 3-Å narrower intersheet distance in 18-28 compared with the other two peptides. Since this analogue is highly soluble in water (Kirschner et al., 1987), the charged residues may be involved in the intersheet interaction. For peptides 17-28 and 15-28, the peaks having higher densities alternate with the ones having lower densities in the H-bonding direction and the dense peaks face less dense peaks located in the *c*-direction (Fig. 7). This arrangement appears to be favorable stereochemically. Although actual assignment of particular side chains will require further refinement of the model, the bulky residues in the 17-28 analogue include Leu_{17}, Phe_{19}, Phe_{20}, and Lys_{28}. Since the addition of Leu_{17} to the 18-28 analogue changed the intersheet distance from ~10 to ~13 Å, these hydrophobic residues may be involved in the intersheet interaction.

Lattice line-like reflections

In the 17-28 β/A4 analogue (Fig. 1 *C*), there were lattice line-like broad reflections off the meridian, and the innermost and strongest reflection was at ~10-Å spacing. Elongation of these reflections along the equatorial direction indicates lattice disorder or a small coherent domain in the direction of the *b*-axis. For peptide 18-28 (Fig. 1 *B*), such broad streaks were not observed, and the lattice constant *c* was 3 Å shorter than that in 17-28. In the pattern from the 15-28 analogue (Fig. 1 *D*) compared with that from 17-28 (Fig. 1 *C*), the lattice line-like reflections were broader, more disordered, and more concentrated on the equator. When the 15-28 samples were dried, the off-meridional reflection became equatorial, and other off-meridional broad reflections were observed at 4.4 and 3.8 Å. These reflections correspond to the (201) and (210) reflections for cross-β crystallites in which the *a*-axis corresponds to the fiber direction.

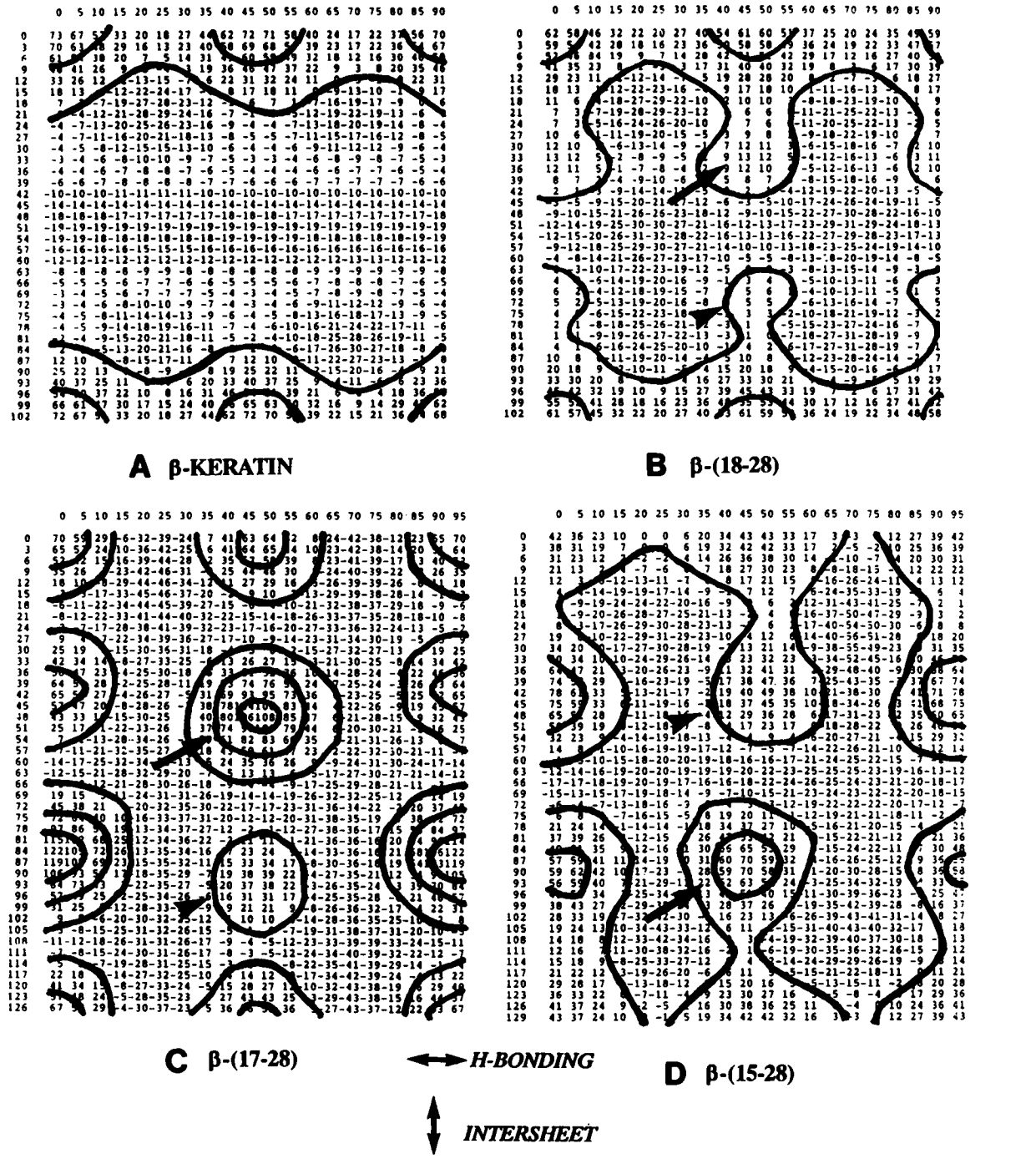

FIGURE 7 Electron density distributions projected onto the *a-c* plane (H-bonding, intersheet plane) along the *b*-axis. (*A*) Original β-keratin model with unit cell dimensions for peptide 18-28. (*B–D*) Refined models for peptide homologues (*B*) 18-28, (*C*) 17-28, and (*D*) 15-28. The *c*-axis (0.3-Å step) is vertical, and the *a*-axis (0.5-Å step) is horizontal. The electron density is on a relative scale and calculated without F(000). Arrows and arrowheads indicate postitions of amino acid sidechains that have high and low electron density, respectively.

Equatorial reflections from periodic stacking of the slabs

The equatorial reflections indexed one dimensionally with periods of 38, 37, and 40 Å for the analogues 18-28, 17-28, and 15-28, respectively (Fig. 1, *B–D*). The first order reflection was very strong, and there was a sudden fall off of the reflections beyond the second order. For the analogues as above, the intensity diminished between 1/40 and 1/20 Å, suggesting that ~30-Å-thick plates are stacked with a ~40-Å period. This size nearly corresponds to β-strands that are 10 residues long in the chain direction. Because the reflections were concen-

TABLE 5 **Positions of new peaks in projected electron intensity from equatorial scatter of plate-like assemblies (Group B)**

Peptide	Peak	x	z
18-28	t	0.010	0.318
	u	0.490	0.318
	v	0.980	0.676
	w	0.511	0.676
17-28	t	0.000	0.310
	u	0.502	0.372
	v	0.000	0.651
	w	0.502	0.713
15-28	t	0.000	0.334
	u	0.503	0.323
	v	0.041	0.680
	w	0.461	0.669

Coordinates in the a-c plane are expressed as fraction of the unit cell dimension. The electron density profiles were refined assuming that the peaks are spheres.

TABLE 7 **Structure factors of meridional pattern from Group B peptide 17-28**

h	k	l	F_{obs}	F_{calc}	Phase	d_{obs}	d_{calc}
0	0	1	41.1	41.3	178.4	12.81	12.89
1	0	0	20.5	22.5	1.4	9.51	9.55
−1	0	1	54.6	52.4	257.3	7.62	7.67
1	0	1	46.7	44.9	274.1	7.62	7.67
0	0	2	19.0	17.6	245.4	6.47	6.45
−1	0	2	65.9	82.5	110.2	5.36	5.34
1	0	2	65.7	82.2	100.6	5.36	5.34
2	0	0	214.6	202.2	359.9	4.78	4.78
0	0	3	130.8	155.3	6.2	4.32	4.30
−1	0	3	48.5	48.2	285.4	3.94	3.92
1	0	3	50.6	50.3	294.8	3.94	3.92
−2	0	3	64.5	30.7	8.6	3.20	3.19
2	0	3	63.3	30.1	9.5	3.20	3.19

Symbols defined as in Table 4. $R_{obs\text{-}amp}$ is 16% and $R_{obs\text{-}int}$ is 26%. The relative error of the integral intensity is 15.7%.

trated on the equator, the plates may be disposed randomly around the axis normal to their surface.

DISCUSSION

New aspects of fiber diffraction analysis

In analyses of fiber diffraction, structure factors are typically obtained from the integral intensity corrected for the Lorentz factor, which includes fiber tilt and disorientation angles (Cella et al., 1970) but not disorder or coherent size. For the current study of x-ray scatter from β/A4 analogues, which contains broad crystalline reflections as well as diffuse scattering, the Lorentz correction for the point-by-point intensity value was defined (see Appendix). The equatorial and meridional intensity curves that we calculated (Figs. 4 and 6) were derived from the intensity plot in film space by setting the ranges of averaging perpendicular to the scanning direction. This procedure is a numerical version of an actual linear scan of the film by a densitometer and allows the calculation of any intensity section in two-dimensional film space. Furthermore, this procedure of working in film space is advantageous for optimizing the atomic coordinates, because noise-enhancing deconvolution is not included.

TABLE 6 **Structure factors of meridional pattern from Group B peptide 18-28**

h	k	l	F_{obs}	F_{calc}	Phase	d_{obs}	d_{calc}
0	0	1	95.5	89.8	6.8	10.36	10.36
0	0	2	47.0	49.9	354.2	5.18	5.18
2	0	0	74.1	71.0	0.0	4.69	4.69
−1	0	2	9.7	6.8	177.8	4.56	4.53
1	0	2	9.8	6.8	357.9	4.56	4.53
−2	0	1	14.7	28.5	8.4	4.26	4.27
2	0	1	14.5	28.0	9.7	4.26	4.27
0	0	3	59.6	60.9	359.2	3.45	3.45

Symbols defined as in Table 4. The $R_{obs\text{-}amp}$ is 14% and the $R_{obs\text{-}int}$ is 15%. The relative error of the observed integral intensity is 14.1%.

Analysis of the x-ray data complements the morphological data

Previous studies of β/A4 analogues depended primarily on electron microscopy for describing the macromolecular morphology. In the current study, analysis of the diffraction patterns indicated two types of macromolecular assembly formed by the analogues: one, a fiber-like structure, and the other, a plate-like structure. The assignment into two types of structures is consistent with the electron microscopic observations of fibrils and ribbons or plates (Castaño et al., 1986; Gorevic et al., 1987; Kirschner et al., 1987; Halverson et al., 1990; Fraser et al., 1991*a, b, c;* Burdick et al., 1992). Our estimates of fiber width from the low-angle equatorial reflections were also consistent with the values from electron microscopy. We had previously noted that the β-keratin atomic coordinates agree with the cell dimensions and the visually estimated intensity for the 1-28 analogue (Kirschner et al., 1987). We have now quantitated the equatorial intensities for 11-28 and found that the atomic coordinates for β-keratin (an antiparallel β-sheet) is, in fact, consistent with the measured x-ray intensities when side chains are included in the model. The intensity of the low-angle equatorial reflections for peptide 1-28 with its apparent 60-Å period had been difficult to measure (Kirschner et al., 1987). By contrast, in the current study this feature was measurable, particularly for peptide 11-28, and allowed us to show that it was consistent with β-crystallite subunits having partially restricted motion and located on a cylindrical lattice. Although this structure is consistent with the electron microscopic observation of the tubular form of amyloid

fiber, this does not emphasize the structural regularity as observed in thin-section electron micrographs of 6-25 peptide (Fraser et al., 1991*a*). By the current model, which assumes local perfect order surrounded by large disorder, the best *R* factor between the observed and calculated intensities was ~30%. It may be necessary to choose a more general formalism, including lattice statistics (lattice disorder parameter), to improve the *R* factor. Such a study will follow the more conventional crystallographic approach after defining the unit cell (as shown in Table 1) and indexing. The β-crystallite structure will give an initial phase model for Fourier synthesis for the 11-28 analogue. The calculated electron density map will address the issue of the assembly of the tubular form of amyloid fibrils in the crystal lattice.

Analysis of the meridional reflections of the plate-like assemblies indicated that the peptide chains are normal to (or tilted) relative to the planar surface, which is in agreement with previous studies on the β/A4 analogues (peptides 16-28 and 18-28) that form ribbon-like structures (Gorevic et al., 1987; Kirschner et al., 1987).

Diversity in macromolecular assembly by β-crystallites

Many naturally occurring protein can form β-structures. Unlike β-amyloid protein, which is abundantly present in AD tissue where it has no known useful role, proteins containing the β-conformation usually do have functional roles. For such proteins, the morphologies can be classified as fiber, rod, tube, ribbon, and plate. The well-known β-forming proteins, β-keratin (Fraser and MacRae, 1962), feather keratin (Fraser et al., 1971), and silk (Marsh et al., 1955*a, b*), form fibers where the β-strands run parallel to the fiber direction. *Chrysopa* (Geddes et al., 1968), by contrast, forms a cross-β form of ribbon where the chains run perpendicular to the fiber direction. Some proteins in viruses (Green et al., 1983) or phage (Earnshaw et al., 1979) show a rod-like appearance of their cross-β arrangements. The proteins that form ion-channels, such as α-toxin (Tobkes et al., 1985) and porin (Kleffel et al., 1985), appear to form oligomers having a β-barrel arrangement in which the chains run normal to the surface of the membrane and the cross-section corresponds to the H-bonding and intersheet directions. This arrangement is not the same as that shown by Group A analogues where the cross-section of cylindrical tube should correspond to the chain and intersheet directions. Although the proposed β-helix for gramicidin (Kennedy, 1978; Koeppe and Kimura, 1984) resembles that of the amyloid proteins with respect to the relative directions of the main chain and the cylindrical tube, this peptide does not form penta- or hexameric oligomers constituted by β-crystallites. The type of plate-like macromolecular assembly exemplified by Group B peptides occurs as synthetic polypeptides when their ionized side chains are neutralized by counter ions such as in poly(*L*-glutamic acid) (Keith et al., 1969), poly(*L*-lysine) (Shmueli and Traub, 1965; Padden et al., 1969), and poly(*L*-arginine) (Suwalsky and Traub, 1972). Usually the membrane-like plates are formed in which the peptide chains run parallel to the surface (e.g., bacterium cell walls in Blaurock and Walsby, 1976; Blaurock and Wober, 1976; Stewart et al., 1985).

Peptide 34-42, which forms thick, twisted cross-β assemblies having dimensions of 85–95 Å by 190–200 Å and pitch 0.12–0.14 μm (Halverson et al., 1990), is unlike the other Group A and C peptides that tend to form narrow and uniform ~60–90-Å-wide fibrils (Fraser et al., 1991*a, b, c*). The ~100-Å intersheet coherent length, which was substantially greater than that of the other peptide assemblies in these groups, and 63 Å width measured from its x-ray pattern likely correspond to the dimensions of the slab-like fibrils that assemble into the twisted fibers. The lateral association of three such slabs in the direction of their polypeptide chains would account for the dimensions of the twisted fibers.

Atomic modeling of β/A4

Atomic models of antiparallel β-pleated sheets in the direction of H-bonding have been proposed in different crystal lattices, namely orthogonal singlet model, with four residues in the unit cell (β-keratin) (Fraser and MacRae, 1962); monoclinic singlet model, with four residues in the unit cell and the sheets staggered uniformly (poly[*L*-glutamic acid]) (Keith et al., 1969); and doublet orthogonal model, with eight residues in the unit cell and the neighboring sheets quarter staggered (silk) (Marsh et al., 1955*a, b*). Various pseudocells such as these were considered for *Chrysopa* fibers (Geddes et al., 1968). In our analysis of the β/A4 analogues, we used the simplest model (orthogonal singlet) and the intersheet lattice constants (*c*-direction) were 10–13 Å, which is in the range of intersheet distances for β-pleated sheets having large side chains (Fraser and MacRae, 1973; see their Table 10.3). It is possible, however, that the doublet orthogonal cell is a unit cell for the fibrillar assemblies (Groups A and C), as previously suggested for the 1-28 analogue (Kirschner et al., 1987) if the ~4.5-Å reflection on the second layer line for some Group A peptides is indexed as a (201) reflection. In this lattice the *c*-direction unit cell is doubled, and this reflection can be very strong in a quarter staggered arrangement of β-sheets.

The molecular schematic of the amyloid fibril that we previously proposed (Kirschner et al., 1987) was based primarily on chemical considerations, with x-ray diffraction and electron microscopic observations for the 1-28 analogue (Kirschner et al., 1987). This model showed nearest neighbor β-sheets arranged antiparallel, both in the H-bonding and intersheet directions, and indicated intermolecular ion pairing between the positively charged His_{13} and the negatively charged Asp_{23} residues. If the neighboring sheets are quarter staggered in the H-

bonding direction, then the lattice becomes similar to that of silk (Marsh et al., 1955*a, b*), and if the β-sheets are moved by one residue along the chain direction, the model shows a similar structure as β-keratin except for the different arrangement (parallel versus antiparallel) in the neighboring sheets (Fraser and MacRae, 1962). In our current analysis, the estimated coherent length suggests that there are only several β-sheets forming the crystallite, and therefore the neighboring sheets may not be exactly in register but disordered.

The model of ion-pair formation appears to be consistent with the observed pH range 3–9 at which the amyloid-type fibrils assemble from peptides 1-28, 9-28, 11-28, and 13-28 (Fraser et al., 1991*c*), and also with the pH range 4–7 at which peptides 1-28, 1-39, and 1-42 form oligomeric β-structures in aqueous trifluoroethanol solution (Barrow and Zagorski, 1991). This model implies that the β-crystallite along the chain direction is ≥11 residues long (~36 Å) and covers the residues from His_{13} to Asp_{23}. This size is consistent with the upper limit of the observed subfibril size based on electron microscopy (Fraser et al., 1991*a, c*) but is too large for the size of the crystallite in the x-ray model for the dehydrated 11-28 analogue analyzed here (see Fig. 5). The smaller size in the chain direction may be better explained by assuming two turns in 11-28 that are centered at residues Gln_{15} and Gly_{25}, according to the protein sequence analysis program described in Inouye and Kirschner (1991), which identified both a minor peak in the β-turn probability curve and a major peak in the β-turn propensity curve. The β-crystallite, therefore, may be composed largely of the hydrophobic residues of Leu_{17}-Val_{18}-Phe_{19}-Phe_{20}-Ala_{21} with the rest of the residues localized to the border region between crystallites. This model suggests, therefore, that hydrophobic interactions predominate in the intersheet direction within the unit crystallites, and that ionic interactions may exist between charged residues in intercrystallite (subfibril–subfibril) interactions. The coherent length of β-sheets in the intersheet direction in 18-28, 17-28, and 15-28, which do not contain His_{13} and His_{14} and which form plate-like structures, ranges from 310 to 410 Å as compared with 32 Å for the 13-28 analogue (Table 2). This suggests that the His residues weaken rather than strengthen the intersheet interactions and thus promotes formation of subfibrils and their pentameric form of assembly.

In conclusion, we have found that a series of β-amyloid analogues displayed diverse macromolecular assemblies that are not commonly observed in naturally occurring proteins. To reconcile analysis of the x-ray diffraction patterns from these assemblies with previous morphological studies on them by electron microscopy, we have proposed that a β-sheet assembly in a plate-like structure can be transformed into a multimeric, hollow cylinder by an alteration in sequence of a few residues. Whether this is true—i.e., that when hydrophilic residues are added to the ends of the hydrophobic core of residues that forms a β sheet, the intersheet interaction will be weakened and subfibrils will form that can assemble into fibrils—is worth considering further for its relevance to understanding in general the folding of proteins into β-structures.

APPENDIX

Glossary

$\mathbf{D}$	position vector in reciprocal the space
D	amplitude of $\mathbf{D}$
R, Φ, Z	cylindrical coordinates in reciprocal space
X, Y, Z	Cartesian coordinates in reciprocal space
μ, χ	longitude and latitude of intersection of scattered x-ray with the Ewald sphere
λ	x-ray wavelength
β	inclination of fiber axis from the normal to the incident x-ray beam (here the positive β directs away from the Ewald sphere)
u, v	Cartesian coordinates on the flat film
s	specimen-to-film distance
2θ	scattering angle
ρ	angle between the fiber axis and the position vector $\mathbf{D}$
$\Delta\rho$	disorientation angle (integral width of the Gaussian distribution)
w	angle between the reflection and the equator on the film
ΔR	integral width of intensity along R direction for the reflection
F	structure factor
f	atomic scattering factor
I	intensity
P	polarization factor
$R_{\text{tot-amp}}$	R factor including all calculated structure amplitudes
$R_{\text{tot-int}}$	R factor including all calculated intensities
$R_{\text{obs-amp}}$	R factor including only observed amplitudes
$R_{\text{obs-int}}$	R factor including only observed intensities

Theory of total intensity function in fiber pattern

X-ray diffraction patterns from the polypeptide assemblies contained both sharp reflections and diffuse scattering. Because separation of the two types of scattering is not straightforward, ideally we should treat the total intensity as a whole in a similar way as we treated the diffraction from nerve myelin for the one-dimensional case by defining the lattice disorder and diffuse scattering (Inouye et al., 1989). In the following the relation between the structure factors and the observed intensity in film space is described for the case when fiber disorientation, fiber tilt, breadth of the reflection due to the limited coherent length, and lattice disorder are present. Use of this film coordinate procedure to simulate fiber diffraction from β-amyloid was previously reported (Fraser et al., 1991*a*).

Relation of film coordinates to reciprocal coordinates

Similar treatments previously have been described (Fraser et al., 1976); however, the earlier description contains some typographical errors. In our notation (see Glossary) the relationship between the flat film coordinates (u, v) and reciprocal vector (R, Z) is

$$u = s \cdot \tan \mu = s \cdot \tan 2\theta \cdot (1 - G^2)^{1/2}$$
$$v = s \cdot \sin \chi / \cos \mu \cdot \cos \chi = s \cdot \tan 2\theta \cdot G, \quad (1)$$

and

$$\sin \chi = \sin 2\theta \cdot G$$
$$\cos \mu \cdot \cos \chi = \cos 2\theta,$$

where $G(\rho) = \cos(\rho)/(\cos\theta \cdot \cos\beta) + \tan\theta \cdot \tan\beta$, $R = D \cdot \sin\rho$, $Z = D \cdot \cos\rho$, and $D = 2 \cdot \sin\theta/\lambda$. Note that the reflections having the same scattering angle are on the circle with radius $(u^2 + v^2)^{1/2} = s \cdot \tan 2\theta$ on the film. Scattering from the reciprocal points (R, Z) occurs on film coordinates (u, v) when the reciprocal point intersects the Ewald sphere. The radial coordinate R, therefore, satisfies the following condition,

$$|\cos\beta/\lambda - V^{1/2}| \le |R| \le |\cos\beta/\lambda + V^{1/2}|, \quad (2)$$

where

$$V = \cos^2\beta/\lambda^2 - Z^2 - 2 \cdot Z \cdot \sin\beta/\lambda.$$

Estimate of fiber tilt

When v_1 and v_2 are the corresponding v-axis film coordinates for the reciprocal points (R, Z) and $(R, -Z)$, the fiber tilt angle β can be found from the observed film coordinates according to

$$\tan\beta = (v_1 + v_2) \cdot (1 - \lambda^2 D^2/2)/s\lambda^2 D^2. \quad (3)$$

Because this equation explicitly includes the film coordinates, it is more straightforward than that of Franklin and Gosling (1953).

Fiber disorientation

The disorientation angle $\Delta\rho$ is defined as the deviation from the mean value of ρ_0. As shown in Eq. 1, the film coordinates (u, v) are related to ρ by G. When v_A and v_B are v-coordinates, the corresponding $\rho = \rho_0 - \Delta\rho$ and $\rho_0 + \Delta\rho$, respectively, and

$$v_A = s \cdot \tan 2\theta \cdot G(\rho_0 - \Delta\rho), \quad \text{and}$$
$$v_B = s \cdot \tan 2\theta \cdot G(\rho_0 + \Delta\rho). \quad (4)$$

When angles between the reflection and the equator (w_A and w_B) are measured, $\sin w_A = G(\rho_0 - \Delta\rho)$ and $\sin w_B = G(\rho_0 + \Delta\rho)$. Then, the $\Delta\rho$ can be obtained according to the following equation

$$\sin\Delta\rho = [\sin(w_A) - \sin(w_B)] \times \cos\beta \cdot \cos\theta/(2 \cdot \sin\rho_0). \quad (5)$$

The density of the molecules is assumed to be distributed along the ρ direction with a Gaussian distribution having an integral width $2\Delta\rho$.

Broadening and disorder

It was assumed here that the limited coherent length along the radial direction broadens the intensity distribution along the R direction in reciprocal space according to a Gaussian distribution having integral width ΔR (see below, Procedure for model calculation). A recent report by Millane and Stroud (1991) is concerned with the first kind of lattice disorder in the radial direction and Clark-Muus type thermal disorder of the atoms. Although these authors derived the intensity function correctly with the given assumptions, the intensity formula is identical to the one given by Tanaka and Naya (1969) except for the lattice disorder term. Inclusion of these disorder parameters gives the diffuse scattering and the reduced intensity of the Bragg peaks. The implementation of these terms in our procedure is straightforward.

Lorentz factor as a function of fiber tilt and fiber disorientation

The total area of an intensity band (S_{band}) that a single reciprocal point may sweep due to fiber rotation and disorientation is

$$S_{band} = (4\pi D^2) \cdot \sin\rho_0 \cdot \sin\Delta\rho. \quad (6)$$

The band intersects the Ewald sphere at two positions and the line length (L_{length}) at each position is

$$L_{length} = (\sin 2\theta/\lambda) \times [a\sin G(\rho_0 - \Delta\rho) - a\sin G(\rho_0 + \Delta\rho)]. \quad (7)$$

Thus, the actual observed integral intensity is reduced by $L' = 2 \cdot L_{length}/S_{band}$ for the rotated fiber having disorientation $\Delta\rho$; this factor is usually called the Lorentz factor. Cella et al. (1970), to account for the finite thickness of the band, reported that $L = L'/\cos\theta$. When the disorientation $\Delta\rho$ is very small and $\rho_0 \neq 0$, L can be approximated as

$$L = \lambda/(2\pi \cdot \sin\theta)/[\cos^2\theta \cdot \cos^2\beta - (\cos\rho_0 + \sin\theta \cdot \sin\beta)^2]^{1/2}. \quad (8)$$

This form has been used (Cella et al., 1970; Fraser and MacRae, 1973; Meader et al., 1980). When the disorientation is still significant at $\rho_0 = 0$, L can be given by substituting $\cos\Delta\rho$ for $\cos\rho_0$ in Eq. 8. This Lorentz factor (L_{merid}) may be used for the observed meridional reflection. For the case of continuous rather than integral intensity, we approximate L' by an infinitely small disorientation,

$$L'_{rot} = \lambda/(2\pi \cdot \tan\theta)/[\cos^2\theta \cdot \cos^2\beta - (\cos\rho + \sin\theta \cdot \sin\beta)^2]^{1/2}. \quad (9)$$

Procedure for model calculation of intensity profile

(*a*) Calculate Miller index, Bragg spacing, and structure factors $F(hkl)$ from atomic coordinates, lattice constants, and atomic factors. The atomic scattering factor can include the Debye factor, which is $\exp(-B \cdot D^2/4)$, where $B = 8\pi^2\delta^2$ and δ is the standard deviation of the atomic center. The δ of a fiber is in the range of 0.25 and 0.44 (Fraser and MacRae, 1973). For our analysis, the atomic scattering factors were calculated from the tabulated coefficients for analytical approximations from the International Tables for X-ray Crystallography (Ibers and Hamilton, 1974). (*b*) Define a fiber axis and calculate the reciprocal coordinates (R_0, Z_0) from the unit cell and Miller indexes. (*c*) Assuming the Gaussian distribution along the R direction $g(R_i, R_0)$ with integral width ΔR and constant Z_0, calculate

$$D_i^2 = R_i^2 + Z_0^2,$$
$$\cos\rho_i = Z_0/D_i, \quad \text{and}$$
$$D_i = 2 \cdot \sin\theta_i/\lambda.$$

(*d*) Assuming a Gaussian distribution along the ρ direction $g(\rho_j, \rho_i)$ with integral width $\Delta\rho$ and constant D_i and θ_i, calculate

$$G(\rho_{j,i}) = \cos(\rho_{j,i})/(\cos\beta \cdot \cos\theta_i) + \tan\theta_i \cdot \tan\beta,$$
$$u(j, i) = s \cdot \tan 2\theta_i \cdot [1 - G(\rho_{j,i})^2]^{1/2}, \quad \text{and}$$
$$v(j, i) = s \cdot \tan 2\theta_i \cdot G(\rho_{j,i}).$$

(*e*) Calculate the intensity on the film coordinates according to

$$I = F(R_0, Z_0)^2 \cdot g(R_i, R_0) \cdot g(\rho_j, \rho_i) \cdot L'_{rot} \cdot P,$$

where the polarization factor $P = [1 + \cos^2(2\theta)]/2$, and L'_{rot} is given by Eq. 9. In typical densitometry, the intensity is linearly scanned. The corresponding intensity from the calculated two-dimensional intensity

map is obtained by defining the ranges of the scan and averaging in the direction normal to the scanning axis.

Analysis of the Bragg reflections in fiber diffraction

The procedure of the total intensity calculation as described above directly relates the model parameters (defined by the atomic coordinates and atomic scattering factors) to the observed intensity in film space. When the observed reflections are sharp, we may use the crystallographic approach without taking into account disorder parameters. When the unit structure is in a three-dimensional lattice (e.g., in a single crystal), the scattered x rays are concentrated at positions defined by $\mathbf{R} = h\mathbf{a}^* + k\mathbf{b}^* + l\mathbf{c}^*$, where h, k, l are integers and $\mathbf{a}^*, \mathbf{b}^*, \mathbf{c}^*$ are reciprocal vectors forming the unit cell. The Fourier transform of the unit cell is sampled by this reciprocal vector and the structure factor $F(h, k, l)$ is written in terms of the atomic scattering factor $f(h, k, l)$,

$$F(h, k, l) = \Sigma_t f_t(h, k, l) \cdot \exp[i2\pi \cdot (hx_t + ky_t + lz_t)], \quad \text{for} \quad l \le t \le n,$$

where n is the number of atoms in the unit cell. The scattered intensity $I(h, k, l) = F(h, k, l)F^*(h, k, l)$, where * denotes conjugate. The structure amplitude $|F(hkl)|$ may be obtained from the *LP*-corrected integral intensity (see Lorentz-polarization correction above) as,

$$|F(hkl)|^2 = (I_{obs}/LP)/m,$$

where m is the multiplicity of reflections giving the same Bragg spacing. In fiber diffraction, I_{obs} is the sum of the intensities of reflections giving the same apparent Bragg spacing. The allowable spacings that contributed to a single reflection were defined by the observed breadth of the reflection. To obtain the structure amplitude from the measured integral intensity, we divided it in proportion to the calculated intensities from the model. The electron density distribution ρ for the unit cell as a function of fractional coordinates u, v, w is

$$\rho(u, v, w) = (1/V)\Sigma_h\Sigma_k\Sigma_l F(h, k, l) \times \exp[-i2\pi \cdot (hu + kv + lw)], \quad \text{for} \quad -\infty \le h, k, l \le +\infty,$$

where V is the volume of the unit cell. Projection of this electron density distribution to a plane or a line gives, respectively,

$$\rho(u, v) = (1/A) \cdot \Sigma_h\Sigma_k F(h, k, 0) \times \exp[-i2\pi \cdot (hu + kv)], \quad \text{and}$$

$$\rho(u) = (1/L) \cdot \Sigma_h F(h, 0, 0) \cdot \exp(-i2\pi \cdot hu),$$

where A is the projected area of the unit cell and L is the length of the unit cell (in the orthogonal case). The three-dimensional electron density distribution was calculated without assuming any particular space group; however, the three-dimensional Fourier calculation may be simplified by Friedel's law. Because the phases of the structure factors were not known, the electron density profile was derived from the observed structure amplitudes and the phases calculated from a model. The initial atomic coordinates were then refined from this profile and the procedure was iterated until the R factor reached an equilibrium. The R factor was defined as

$$R_{amp} = \Sigma|\,|F_{obs}| - |F_{calc}|\,|/\Sigma|F_{obs}|$$

$$R_{int} = \Sigma|I_{obs} - I_{calc}|/\Sigma|I_{obs}|,$$

where $I_{obs} = |F_{obs}|^2$ was scaled to satisfy $\Sigma I_{obs} = \Sigma I_{calc}$ for both R factors. When the above summation is taken over all calculated indices, the R factor includes not only the observed intensities but also the unobserved intensities. In our nomenclature $R_{tot\text{-}amp}$ refers to the R factor using all calculated reflections, whereas $R_{obs\text{-}amp}$ refers to the R factor using only the observed reflections.

We thank Drs. Larry Duffy, Blas Frangione, and Peter Lansbury for providing us with some of the synthetic peptides, and Jack T. Nguyen for assistance with some of the x-ray diffraction experiments. The FORTRAN packages used in film scanning and display were originally developed in the Image Graphics Laboratory (IGL), Neurology Research, Children's Hospital, for the three-dimensional reconstruction of neuroanatomic and autoradiographic data. We thank our IGL colleagues over the years (Linda Kirschner, Josh Simons, and Monty Brandenberg) for providing the source code for these programs so that they could be adapted to our own applications. Most of the calculations were done on the IGL's DEC 11/780 VAX computer using the VAX/VMS operating system. Additional calculations were done using a DECStation 5000/200PXG workstation with the UNIX operating system, which was set up in our laboratory by Dr. Tom Tibbitts. Finally, we are grateful to the succession of IGL system managers Gene Belch, Josh Simons, Nariman Shambayati, Gene Zilberstein, and Rob Cornette for their continued assistance.

The research was supported in part by the American Federation for Aging Research (to D. A. Kirschner), American Health Assistance Foundation (to D. A. Kirschner), and National Institutes of Health grant AG-08572 (to D. A. Kirschner) from the National Institute of Aging. Dr. Fraser was a postdoctoral fellow of the Medical Research Council of Canada. Some of the work was carried out in facilities related to the Mental Retardation Research Center of Children's Hospital and was supported by Core grant HD-18655 from the National Institutes of Health.

Received for publication 11 June 1992 and in final form 17 September 1992

REFERENCES

Barrow, C. J., and M. G. Zagorski. 1991. Solution structures of beta peptide and its constituent fragments: relation to amyloid deposition. *Science (Wash. DC)*. 253:179–182.

Blaurock, A. E. and A. E. Walsby, 1976. Crystalline structure of the gas vesicle wall from *Anabaena flos-aquae*. *J. Mol. Biol.* 105:183–199.

Blaurock, A. E. and W. Wober. 1976. Structure of the wall of *Halobacterium halobium* gas vesicles. *J. Mol. Biol.* 106:871–888.

Burdick, D., B. Soreghan, M. Kwon, J. Kosmoski, M. Knauer, A. Henschen, J. Yates, C. Cotman, and C. Glabe. 1992. Assembly and aggregation properties of synthetic Alzheimer's A4/β amyloid peptide analogs. *J. Biol. Chem.* 267:546–554.

Burge, R. E. 1961. The structure of bacterial flagella: the packing of the polypeptide chains within a flagellum. *Proc. R. Soc. (Lond.)*. A260:558–573.

Castaño, E. M., J. Ghiso, F. Prelli, P. D. Gorevic, A. Migheli, and B. Frangione. 1986. In vitro formation of amyloid fibrils from two synthetic peptides of different lengths homologous to Alzheimer's disease β-protein. *Biochem. Biophys. Res. Commun.* 141:782–789.

Cella, R. J., B. Lee, and R. E. Hughes. 1970. Lorentz and orientation factors in fiber x-ray diffraction analysis. *Acta Crystallogr.* A26:118–124.

Chothia, C. 1984. Principles that determine the structure of proteins. *Annu. Rev. Biochem.* 53:537–572.

Chou, K.-C., G. Nemethy, and H. A. Scheraga. 1983. Role of interchains in the stabilization of the right-handed twist of β-sheets. *J. Mol. Biol.* 168:389–407.

Earnshaw, W. C., E. B. Goldberg, and R. A. Crowther. 1979. The distal half of the tail fibre of bacteriophage T4. Rigidly linked domains and cross-β structure. *J. Mol. Biol.* 132:101–131.

Franklin, R. E. and R. G. Gosling. 1953. The structure of sodium thymonucleate fibres. II. The cylindrically symmetrical Patterson function. *Acta Crystallogr* 6:678–685.

Fraser, P. E., L. K. Duffy, M. B. O'Malley, J. Nguyen, H. Inouye, and D. A. Kirschner. 1991*a*. Morphology and antibody recognition of synthetic β-amyloid peptides. *J. Neurosci. Res.* 28:474–485.

Fraser, P. E., H. Inouye, J. Nguyen, K. Halverson, P. T. Lansbury, L. K. Duffy, and D. A. Kirschner. 1991*b*. Morphology, conformation and stability of Alzheimer β-amyloid peptide fibrils. *In* Expanding Frontiers in Polypeptide and Protein Structural Research. V. Renugopalakrishnan, P. R. Carey, I. C. P. Smith, S. G. Huang, and A. C. Storer, editors. ESCOM, Leiden, The Netherlands. 309–315.

Fraser, P. E., J. Nguyen, W. K. Surewicz, and D. A. Kirschner. 1991*c*. pH-dependent structural transitions of Alzheimer amyloid peptides. *Biophys. J.* 60:1190–1201.

Fraser, R. D. B. and T. P. MacRae. 1962. An investigation of the structure of β-keratin. *J. Mol. Biol.* 5:457–466.

Fraser, R. D. B., and T. P. MacRae. 1973. Conformation in Fibrous Proteins. Academic Press, New York. 628 pp.

Fraser, R. D. B., T. P. MacRae, D. A. D. Parry, and E. Suzuki. 1971. The structure of feather keratin. *Polymer* 12:35–56.

Fraser, R. D. B., T. P. MacRae, A. Miller, and R. J. Rowlands. 1976. Digital processing of fibre diffraction patterns. *J. Appl. Crystallogr.* 9:81–94.

Geddes, A. J., K. D. Parker, E. D. T. Atkins, and E. Beighton. 1968. "Cross-β" conformation in proteins. *J. Mol. Biol.* 32:343–358.

Gorevic, P. D., E. M. Castaño, R. Sarma, and B. Frangione. 1987. Ten to fourteen residue peptides of Alzheimer's disease protein are sufficient for amyloid fibril formation and its characteristic x-ray diffraction pattern. *Biochem. Biophys. Res. Commun.* 147:854–862.

Green, K. M., N. G. Wrigley, W. C. Russell, S. R. Martin, and A. D. McLachlan. 1983. Evidence for a repeating cross-β sheet structure in the adenovirus fibre. *EMBO (Eur. Mol. Biol. Organ.) J.* 2:1357–1365.

Guinier, A., and G. Fournet. 1955. Small-angle scattering of x-rays. John Wiley and Sons, Inc., New York.

Halverson, K., P. E. Fraser, D. A. Kirschner, and P. T. Lansbury, Jr. 1990. Molecular determinants of amyloid deposition in Alzheimer's disease: conformational studies of synthetic β-protein fragments. *Biochemistry.* 29:2639–2644.

Heyn, A. N. J. 1948. Small angle x-ray scattering of various cellulose fibers. *J. Am. Chem. Soc.* 70:3138–3139.

Hilbich, C., B. Kisters-Woike, J. Reed, C. L. Masters, and K. Beyreuther. 1991. Aggregation and secondary structure of synthetic amyloid βA4 peptides of Alzheimer's disease. *J. Mol. Biol.* 218:149–163.

Ibers, J. A., and W. C. Hamilton, editors. 1974. International Tables for X-ray Crystallography. Vol. IV. The Kynoch Press, Birmingham, England. 366 pp.

Inouye, H., J. Karthigasan, and D. A. Kirschner. 1989. Membrane structure in isolated and intact myelins. *Biophys. J.* 56:129–137.

Inouye, H., P. E. Fraser, and D. A. Kirschner. 1991. Beta-crystallite assemblies of Alzheimer beta-amyloid protein homologues. *Proc. Am. Crystallogr. Assoc.* 19:84.

Inouye, H., and D. A. Kirschner. 1991. Folding and function of the myelin proteins. *J. Neurosci. Res.* 28:1–17.

Keith, H. D., F. J. Padden, Jr., and G. Giannoni. 1969. Crystal structures of β-poly-L-glutamic acid and its alkaline earth salts. *J. Mol. Biol.* 43:423–438.

Kennedy, S. J. 1978. Structures of membrane proteins. *J. Membr. Biol.* 42:265–279.

Kirschner, D. A., C. Abraham, and D. J. Selkoe. 1986. X-ray diffraction from intraneuronal paired helical filaments and extraneuronal amyloid fibers in Alzheimer disease indicates cross-β conformation. *Proc. Natl. Acad. Sci. USA.* 83:503–507.

Kirschner, D. A., H. Inouye, L. K. Duffy, A. Sinclair, M. Lind, and D. J. Selkoe. 1987. Synthetic peptide homologous to β protein from Alzheimer disease forms amyloid-like fibrils in vitro. *Proc. Natl. Acad. Sci. USA.* 84:6953–6957.

Kleffel, B., R. M. Garavito, W. Baumeister, and J. P. Rosenbusch. 1985. Secondary structure of a channel-forming protein: porin from *E. coli* outer membranes. *EMBO (Eur. Mol. Biol. Organ.) J.* 4:1589–1592.

Koeppe, R. E., II, and M. Kimura. 1984. Computer building of β-helical polypeptide models. *Biopolymers.* 23:23–38.

Marsh, R. E., R. B. Corey, and L. Pauling. 1955*a*. An investigation of the structure of silk fibroin. *Biochim. Biophys. Acta.* 16:1–34.

Marsh, R. E., R. B. Corey, and L. Pauling. 1955*b*. The structure of Tussah silk fibroin. *Acta Crystallogr.* 8:710–715.

Marvin, D. A., M. Spencer, M. H. F. Wilkins, and L. D. Hamilton. 1961. The molecular configuration of deoxyribonucleic acid. III. X-ray diffraction study of the C form of the lithium salt. *J. Mol. Biol.* 3:547–565.

Meader, D., E. D. T. Atkins, M. Elder, P. A. Machin, and M. Pickering. 1980. AXIS: a semi-automated x-ray intensity and d-spacing analyser for fiber diffraction patterns. *In* Fiber Diffraction Methods. A. D. French and K. H. Gardner, editors. ACS Symposium Series #141, Washington, D.C. 113–138.

Millane, R. P., and W. J. Stroud. 1991. Effects of disorder on fibre diffraction patterns. *Int. J. Biol. Macromol.* 13:202–208.

Miller, A. and J. S. Wray. 1971. Molecular packing in collagen. *Nature (Lond.).* 230:437–439.

Oster, G. and D. P. Riley. 1952. Scattering from cylindrically symmetric systems. *Acta Crystallogr.* 5:272–276.

Padden, F. J., Jr., H. D. Keith, and G. Giannoni. 1969. Single crystals of poly-L-lysine. *Biopolymers.* 7:793–804.

Shmueli, U., and W. Traub. 1965. An x-ray diffraction study of poly-L-lysine hydrochloride. *J. Mol. Biol.* 12:205–214.

Stewart, M., T. J. Beveridge, and G. D. Sprott. 1985. Crystalline order to high resolution in the sheath of *Methanospirillum hungatei:* a cross-β structure. *J. Mol. Biol.* 183:509–515.

Suwalsky, M. and W. Traub. 1972. An x-ray diffraction study of poly-L-arginine hydrochloride. *Biopolymers.* 11:623–632.

Tanaka, S. and S. Naya. 1969. A theory of x-ray scattering by disordered polymer crystals. *J. Physical Soc. Jpn.* 26:982–993.

Tobkes, N., B. A. Wallace, and H. Bayley. 1985. Secondary structure and assembly mechanism of an oligomeric channel protein. *Biochemistry.* 24:1915–1920.

Vainshtein, B. K. 1966. Diffraction of x-rays by chain molecules. Elsevier Publishing Company, Amsterdam, The Netherlands. 414 pp.

Waser, J. 1955. Fourier transforms and scattering intensities of tubular objects. *Acta Crystallogr* 8:142–150.

Worthington, C. R., and H. Inouye. 1985. X-ray diffraction study of the cornea. *Int. J. Biol. Macromol.* 7:2–8.

Zimmerman, J. M., N. Eliezer, and R. Simha. 1968. The characterization of amino acid sequences in proteins by statistical methods. *J. Theor. Biol.* 21:170–201.